Evidence of a Transient Ozone Depletion Event in the Early Hunga Plume Above the Indian Ocean

Tristan Millet [1], Hassan Bencherif [1], Thierry Portafaix [1], Nelson Bègue [1], Alexandre Baron [2], Valentin Duflot [1,*], Cathy Clerbaux [3,4], Pierre-François Coheur [4], Andrea Pazmiño [3], Michaël Sicard [1,5], Anne Boynard [3,6], Jean-Marc Metzger [7], Guillaume Payen [7], Nicolas Marquestaut [7], and Sophie Godin-Beekmann [3]

[1]LACy, Laboratoire de l'Atmosphère et des Cyclones (UMR 8105 CNRS, Université de La Réunion, Météo-France) Saint-Denis de La Réunion, France
[2]Cooperative Institute for Research in Environmental Sciences, and NOAA Chemical Sciences Laboratory, Boulder, USA
[3]LATMOS/IPSL, Sorbonne Université, UVSQ, CNRS, Paris, France
[4]Spectroscopy, Quantum Chemistry and Atmospheric Remote Sensing, Université Libre de Bruxelles (ULB), Brussels, Belgium
[5]CommSensLab-UPC, Universitat Politècnica de Catalunya, Barcelona, Spain
[6]SPASCIA, Ramonville-Saint-Agne, 31520, France
[7]Observatoire des Sciences de l'Univers de La Réunion (OSUR), CNRS/Université de La Réunion/Météo-France, UAR 3365, Saint-Denis, France
[*]now at : Department for Atmospheric and Climate Research, NILU – Norwegian Institute for Air Research, Kjeller, Norway
Correspondence: Tristan Millet (tristan.millet@univ-reunion.fr)

Abstract. On 15 January 2022, the Hunga volcano (20.5° S, 175.4° E) erupted, releasing significant amounts of water vapor (H_2O) and a moderate quantity of sulfur dioxide (SO_2) into the stratosphere. The resulting volcanic plume traveled westward with the southern hemispheric stratospheric circulation, reaching the Indian Ocean and Reunion (21.1° S, 55.5° E) within days. This study presents the first analysis of Infrared Atmospheric Sounding Interferometer (IASI) ozone data to investigate the impact of the Hunga eruption, and also incorporates Microwave Limb Sounder (MLS) and Ozone Mapping and Profiler Suite Limb Profiler (OMPS-LP) data, as well as ground-based measurements from Reunion. IASI observations revealed a transient ozone depletion event in the first week following the eruption. OMPS-LP aerosol extinction profiles, sun-photometer measurements, and lidar observations characterized the plume's vertical and latitudinal extent, showing its presence over Reunion at altitudes ranging from 26.8 to 29.7 km and its spread across more than 30° longitude and 20° latitude by 21 January. IASI ozone spatial distributions showed marked decreases in total and stratospheric ozone on that date, with the 5th percentile of the anomaly reaching -18.6 DU for Total Column Ozone (TCO) and -14.5 DU for Stratospheric Column Ozone (SCO). A key finding, as shown by MLS profiles, is that the ozone reduction was confined to two separate layers (-0.7 $\pm$ (1σ) 0.6 ppmv in the 14.68–12.12 hPa range, and -0.6 $\pm$ (1σ) 0.5 ppmv in the 31.62–21.54 hPa range), each associated with a distinct aerosol cloud with excess H_2O. This layered structure of ozone loss offers new insight into the chemical and radiative effects of the Hunga plume on stratospheric ozone.

1   Introduction

Due to its high oxidizing potential and contribution to the radiative budget, ozone plays an undeniable role in the Earth's atmosphere (IPCC, 2013, 2021; WMO, 2022). In the stratosphere, ozone serves as a protective shield for the biosphere by absorbing the majority of solar ultraviolet radiation in the 280–315 nm range (Orphal et al., 2016). This shielding action protects ecosystems and human health from the harmful effects of UV-B radiation, which can lead to adverse health issues such as cataracts, melanoma, and skin aging, while deteriorating materials (Pitts et al., 1977; Matsumura and Ananthaswamy, 2004; Bernhard et al., 2020; Neale et al., 2021). In the past decades, anthropogenic emission of chlorofluorocarbons (CFCs) and halons (including Br) was found to be responsible for the rapid decline in stratospheric ozone (Molina and Rowland, 1974; Solomon, 1988; Rowland, 1996). Within the stratosphere, CFCs are indeed photo-dissociated into chlorine compounds which are known to efficiently deplete ozone (Solomon, 1999). Following the ratification of the Montreal Protocol in 1987, CFC emissions were gradually restricted and forbidden, and previous research and reports show that the ozone layer is expected to return to its 1970s levels from the middle to the end of this century, depending on the latitude (Dhomse et al., 2018; WMO, 2022).

In contrast, tropospheric ozone is a secondary pollutant that directly harms ecosystems, reduces crop productivity, and has negative effects on human health (Mills et al., 2018; Nuvolone et al., 2018). Photochemical formation of tropospheric ozone is driven by the combination of solar radiation and ozone precursors, including volatile organic compounds (VOCs), nitrogen oxides (NO_x) and aerosols (Jacob, 1999; Ivatt et al., 2022). Ozone in the troposphere can therefore be enhanced by anthropogenic activities that release NO_x, aerosols and VOCs, such as agriculture, industry and transport.

Explosive volcanic eruptions can influence stratospheric ozone concentrations, and thus play a role in global atmospheric chemistry and radiative forcing (Robock, 2000). Previous major eruptions, such as those of Fuego (1974), El Chichón (1982), Mount Pinatubo (1991), Cerro Hudson (1991) and Calbuco (2015), are well-documented examples of events that have altered global atmospheric chemistry (Crafford, 1975; Cadle et al., 1977; Doiron et al., 1991; Gobbi et al., 1992; Schoeberl et al., 1993; McCormick et al., 1995; WMO, 1999; Guo et al., 2004; Kremser et al., 2016; Zhu et al., 2018). Explosive eruptions can release substantial amounts of sulfur dioxide (SO_2), which is subsequently converted into sulfuric acid (H_2SO_4). The resulting sulfuric acid condenses to form sulfate aerosols, secondary volcanic particles which can in turn contribute to stratospheric ozone depletion by increasing the surface area available for heterogeneous reactions. Studies have highlighted the relationship between SO_2 and chlorine in causing ozone decline post-eruption (e.g. Hofmann and Solomon (1989); Tie and Brasseur (1995)). As an example, McCormick et al. (1995) reported that tropical column ozone decreased by 6–8 % in the months following the Mount Pinatubo eruption. They observed that losses were greatest below 28 km, amounting to 20 % in the 24–25 km altitude range. Because of the resulting ozone losses and radiative forcing anomalies, the injection of volcanic plumes into the stratosphere can also influence atmospheric temperatures. Ramaswamy et al. (2006) observed increases in global lower stratospheric temperatures following the major eruptions of El Chichón and Mount Pinatubo. Moreover, it was determined that the ozone depletion in the aerosol layer caused by the Mount Pinatubo eruption reduced stratospheric heating by 30 %

(Kirchner et al., 1999). Despite this reduction, the radiative anomalies caused by the presence of stratospheric aerosols induced a global stratospheric warming of 3–4 K and tropospheric cooling (Stenchikov et al., 1998; Kirchner et al., 1999).

Moderate and major eruptions may also contribute to the amplitude and dimension of the ozone hole over Antarctica. Following the Mount Pinatubo eruption, Hofmann and Oltmans (1993) observed unusually low total ozone values of 105 DU over the South Pole Station. This deeper ozone hole was attributed to enhanced polar stratospheric cloud (PSC) volume driven by extra stratospheric sulfuric acid availability, offering more particle surfaces for heterogeneous reactions. Ivy et al. (2017) reported an increase of the 2015 Antarctic ozone hole by 4.5×10^6 km^2, primarily attributed to volcanic aerosols from the Calbuco eruption. Similarly, Zhu et al. (2018) reported penetration of volcanic sulfate aerosols from the Calbuco eruption into the Antarctic polar vortex, resulting in earlier ozone loss and an increase in the area of the ozone hole. Yook et al. (2022) also hypothesized a link between the eruption of La Soufrière in 2021 and the longevity of the 2021 ozone hole. Hence, numerous research papers focused on ozone chemistry and atmospheric forcings following eruption events.

The Hunga eruption constitutes an unprecedented event of the satellite era (Wright et al., 2022; Carr et al., 2022). The main eruption likely released more energy than the 1991 Mount Pinatubo eruption and caused the largest stratospheric aerosol disturbance since that event (Sellitto et al., 2022; Khaykin et al., 2022; Taha et al., 2022). Its consequences have been under intensive scrutiny, and studies revealed it injected $\sim$0.5 Tg of SO$_2$ and 146 ± 5 Tg of water vapor (H$_2$O) into the stratosphere, corresponding to an increase of $\sim$10 % of the global stratospheric H$_2$O burden (Khaykin et al., 2022; Vömel et al., 2022; Zuo et al., 2022; Millán et al., 2022). The eruption's aerosol column extended through the troposphere and stratosphere, and even reached the lower mesosphere (Carr et al., 2022). Legras et al. (2022) demonstrated that the initial volcanic plume consisted of two distinct sulfate aerosol clouds, which descended from $\sim$30 and $\sim$28 km on 15 January to $\sim$27 and $\sim$25 km by 28 January.

Evan et al. (2023) and Zhu et al. (2023) attribute the initially low ozone levels observed in satellite data to the lofting of ozone-poor tropospheric air masses. However, the subsequent ozone depletion in the following days is attributed to chemical processes, particularly heterogeneous chlorine activation on humidified volcanic aerosols. The significant increase in stratospheric humidity facilitated the rapid conversion of SO$_2$ to sulfate aerosols in less than two weeks (Legras et al., 2022; Zhu et al., 2022; Asher et al., 2023; Zhu et al., 2023), increasing aerosol surface area. This, combined with Hunga-induced stratospheric cooling (Sellitto et al., 2022; Coy et al., 2022; Schoeberl et al., 2022; Sicard et al., 2025), enhanced heterogeneous reaction rates, likely accelerating chlorine activation on sulfate aerosols and leading to notable ozone depletion despite elevated non-polar temperatures (Evan et al., 2023; Zhu et al., 2023). In this context, Evan et al. (2023) provided evidence of HCl activation on sulfate aerosols within the fresh volcanic plume, and Zhu et al. (2023) elucidated the mechanisms giving rise to the changes observed immediately following the event. (For completeness, note that comprehensive discussions of the stratospheric chemical processes at work in subsequent months can be found in Wilmouth et al. (2023), Santee et al. (2023) and Zhang et al. (2024)).

While heterogeneous reactions played a crucial role in ozone loss, Zhu et al. (2023) also emphasized the importance of gas-phase reactions. In fact, Zhu et al. (2023) and Evan et al. (2023) identified key gas-phase mechanisms contributing to ozone loss: enhanced HO$_x$ cycle activity due to high H$_2$O concentrations, as highlighted by Wilmouth et al. (2023), strengthened interactions between the HO$_x$ and ClO$_x$ cycles (through HO$_2$ + ClO $\rightarrow$ HOCl + O$_2$), and the slowing down of the NO$_x$ cycle.

Thus, the substantial increase in the rates of key reactions led to a 5 % decrease in stratospheric ozone over the Indian Ocean within a week of the eruption, as reported by Evan et al. (2023), with the most pronounced losses occurring during peak stratospheric humidification.

This study provides the first analysis of ozone observations using Infrared Atmospheric Sounding Interferometer (IASI) (Aires et al., 2002; Blumstein et al., 2004) data following the January 2022 Hunga eruption, focusing on the Indian Ocean and particularly Reunion, where our ground-based measurements are performed. Due to the prevailing westward austral summer stratospheric circulation, the first signs of the Hunga plume's passage over Reunion were noticed only 4 days after the eruption (Legras et al., 2022; Baron et al., 2023). This study combines local ground-based measurements at Reunion with satellite data over the Indian Ocean, including observations from the Microwave Limb Sounder (MLS) (Waters et al., 2006) and IASI, to examine the impacts of Hunga on ozone during the first 10 days post-eruption. The goal is not to elucidate the chemical mechanisms giving rise to the observed low ozone, as they were investigated in detail by Evan et al. (2023) and Zhu et al. (2023). Rather, the objectives of the present manuscript can be summarized in three points: firstly, we use IASI observations to demonstrate the appearance of a transient ozone depletion event; secondly, we show the zonal displacement of the SO_2 and H_2O plumes using satellite data; and thirdly, we use MLS ozone profiles obtained within each of the two Hunga clouds to characterize their respective impacts on ozone.

2 Instrumentation and Method

In this study, we combined ground-based and satellite observational data to investigate the impacts on ozone after the Hunga eruption. This work focuses on the region bounded by 45° E to 175° E and 30° S to 0° and relies exclusively on satellite measurements from this area. This section outlines the different types of data used in our analysis. Unless specified otherwise, all uncertainties, standard errors and standard deviations are reported at the 2σ confidence level.

2.1 Ozone measurements

2.1.1 Lidar

A stratospheric DIfferential Absorption Lidar (DIAL) has been operated since January 2013 at the Reunion Atmospheric Physics Observatory (OPAR, 21.08° S; 55.38° E, 2160 m asl) (Baray et al., 2013; Portafaix et al., 2015). This instrument can retrieve ozone concentration profiles at altitudes ranging from 15 to ∼45 km. Lidar observations provide high vertical resolution (Pazmiño, 2006), with typical values ranging from 0.5 km at 15 km to 5 km at 45 km (Godin-Beekmann et al., 2003). The total accuracy is ∼5 % below 20 km, ∼3 % in the 20–30 km altitude range and 15–30 % above 45 km (Godin-Beekmann et al., 2003). However, although the Maïdo DIAL system recorded data during the initial passage of the volcanic plume in January 2022, the corresponding signal-to-noise ratio (SNR) was extremely low, and the ozone profiles were not reliable. As a result, stratospheric DIAL ozone profiles used in this paper were recorded before the Hunga eruption, from January 2013 to December 2021. The 470 ozone profiles obtained during this period were used to determine the background ozone level for the

month of January and were compared with profiles from satellites. As part of the Network for the Detection of Atmospheric Composition Change (NDACC), this DIAL data can be accessed from the NDACC website (https://ndacc.larc.nasa.gov/, last accessed on 10 March 2025).

2.1.2 SAOZ

The Système d'Analyse par Observation Zénithale (SAOZ), an instrument also integrated into the NDACC, is a ground-based spectrometer which measures the sunlight scattered from the zenith sky within the 300 to 650 nm range (Pommereau and Goutail, 1988). Differential Optical Absorption Spectrometry (DOAS) is utilized to analyze observations, enabling the retrieval of daily ozone and nitrogen columns at sunrise and sunset with a total accuracy of 6 % and 14 %, respectively (Boynard et al., 2018). Operating at an altitude of 80 m asl in Saint-Denis (20.90° S; 55.48° E), Reunion, since 1993, a SAOZ instrument has provided Total Column Ozone (TCO) observations at this subtropical site for over three decades. Unfortunately, SAOZ data during the passage of the aerosol plume over Reunion are unreliable because of an unrealistic representation of the Air Mass Factor (AMF), leading to biased TCO retrievals. Consequently, SAOZ data for January 2022 were excluded. However, data outside this time period and climatological values of TCO for the month of January (262.8 ± 11.9 DU) were kept to illustrate the background January TCO. The dataset used in this work can be downloaded from the SAOZ website (http://saoz.obs.uvsq.fr/, last accessed on 10 March 2025).

2.1.3 MLS

The MLS instrument is aboard the Aura satellite, which was launched in July 2004. The Aura satellite follows a helio-synchronous orbit and passes the equator at 13:45 local solar time on its ascending node. In order to observe atmospheric parameters like temperature and atmospheric component concentrations, MLS measures thermal radiation emitted from the Earth's atmospheric limb ahead of its orbital path at spectral wavelengths ranging from 0.12 to 2.5 mm (Waters et al., 2006). According to Millán et al. (2022), MLS version 4 (v4) level 2 data should be used to study conditions within the fresh Hunga plume for the first weeks after the eruption instead of the latest version (v5). Indeed, the extraordinary H_2O enhancement from Hunga compromised the accuracy of some v5 MLS data products during the first few weeks after the eruption. However, their study indicates that the quality of MLS ozone and temperature measurements are not affected by the volcanic plume (Millán et al., 2022).

Following the recommendations of Millán et al. (2022), the MLS profiles for January 2022 are sourced exclusively from level 2 v4 measurements (Livesey et al., 2020). The MLS profiles are categorized as Hunga-influenced or non-influenced using criteria detailed in the next paragraph. To evaluate the similarity between v4 and v5 MLS ozone profiles during background atmospheric conditions, we calculated the differences for the colocated v4 and v5 non-influenced ozone profiles. The maximum standard deviation did not exceed 0.1 ppmv on any of the 10 to 100 hPa pressure levels, corresponding to a 0.02% variation relative to the mean ozone volume mixing ratio in this region, demonstrating the similarity of these two versions during background conditions. Additionally, to assess the similarity between v5 MLS ozone profiles and the Reunion DIAL profiles, we performed an inter-comparison procedure detailed in Section 2.4. To compare v4 Hunga-influenced ozone profiles to back-

ground non-influenced profiles, we employed MLS level 2 v5 data (Livesey et al., 2022). All v5 ozone and water vapor profiles (on both ascending and descending sides of the orbit) within a 5-degree radius of each of the January 2022 Hunga-influenced profiles were collected. This procedure was undertaken for each day for the months of January from 2013 to 2021 to derive the monthly averaged background profiles. This specific time period was chosen to align with the lidar time series.

The selection of v4 MLS Hunga-influenced profiles follows an adaptation of the criterion from Evan et al. (2023). First, similar to their procedure, locations with v4 water vapor profiles exhibiting mixing ratio values exceeding 100 ppmv within the 10 to 100 hPa range were identified. Based on Legras et al. (2022), the criterion was then refined to classify as Hunga-influenced only those profiles affected by one of the two sulfate aerosol clouds located at approximately 25 km and 28 km (corresponding to the 26.10 and 14.68 hPa MLS pressure levels, respectively). Specifically, only profiles in which the maximum H_2O anomaly occurs at one of these two pressure levels were considered as Hunga-influenced. This refinement accounts for the fact that, during the study period (15–23 January 2022), water vapor and aerosol plumes were colocated before diverging due to particle sedimentation. These two separate plumes of water vapor and aerosols are referred to as "Hunga clouds". As a result, locations with peak water vapor at either of these pressure levels were classified as Hunga-influenced. Applying this refined criterion yielded 47 Hunga-influenced and 2266 non-influenced ozone and water vapor profiles between 15 and 23 January 2022 over the Indian Ocean. Of the Hunga-influenced profiles, 26 were impacted by the higher-altitude cloud, and 21 by the lower-altitude one. The two profile groups were analyzed separately to characterize the individual impacts of each Hunga cloud on ozone.

In most of the stratosphere, specifically between 1 and 68 hPa, MLS ozone volume mixing ratio profiles have accuracy and precision that are both better than 10 % (Livesey et al., 2022). In accordance with the recommendations made in the MLS data quality and description documents, all quality flags (quality, convergence, status and precision) were used on the raw profiles (with the exception of the v4 and v5 H_2O profiles), and data lying outside the recommended range (261 to 0.001 hPa, or approximately 11 to 90 km) were not used (Livesey et al., 2020, 2022). MLS observations can be accessed through NASA's data portal (https://disc.gsfc.nasa.gov/, last accessed on 10 March 2025).

2.1.4 IASI

In 2006, the first Infrared Atmospheric Sounding Interferometer (IASI) was launched aboard the Metop-A satellite (Clerbaux et al., 2009; Coheur et al., 2009). A second instrument was launched in 2012 on Metop-B, followed by a third on Metop-C in 2018. These satellites operate in a polar orbit, providing global observations twice a day (09:30 and 21:30 local time) for weather prediction and climate monitoring. IASI is a Fourier transform spectrometer, which measures the radiation emitted by the Earth-atmosphere system in the thermal infrared (645–2760 cm^{-1} or 3.62–15.5 μm) across 8461 spectral channels, with a resolution of 0.25 cm^{-1} (0.5 cm^{-1} after apodization). IASI's swath covers 30 fields of view, each containing 4 pixels, allowing for complete Earth coverage during each pass.

In this study we used the IASI ozone profiles retrieved from the Fast-Optimal Retrievals on Layers for IASI (FORLI) (Hurtmans et al., 2012), which have been extensively validated (Boynard et al., 2018) and which are available to users on the AERIS website (https://iasi.aeris-data.fr, last accessed on 10 March 2025). The ozone product is a vertical profile given as partial columns in molecules cm^{-2} in 40 layers between the surface and 40 km, with an extra layer from 40 km to ∼60 km. To

ensure that only the most reliable observations are used in our analysis, we applied a filtering process, retaining only profiles and columns with more than two degrees of freedom and a retrieval quality filter equal to 1, as recommended by (Boynard et al., 2018). We analyzed both the TCO and Stratospheric Column Ozone (SCO) products. The latter is derived by summing the ozone partial columns from the thermal tropopause, estimated from the IASI temperature profiles using the WMO definition (WMO, 1957), to ∼60 km.

As Metop-A began its orbital drift in 2017 and stopped providing measurements in 2021, only IASI/Metop-B and -C have been used in this study. To facilitate the analysis, the IASI TCO and SCO data were first averaged daily over a $1° \times 1°$ global grid. The background ozone levels were defined as the daily average of IASI/Metop-B data from 2014 to 2021. The daily ozone values for 2022 were derived from both Metop-B and -C to maximize the number of data points. IASI TCO and SCO anomalies were defined as the difference between the daily ozone levels in January 2022 and the background daily ozone (average between 2014 and 2021 for January). To ensure statistical reliability for the ozone anomalies, only grid points with at least three observations were considered.

To complement the analysis, we also included daily SO_2 measurements from IASI/Metop-B and -C (Clarisse et al., 2012, 2014). Regional ozone anomalies were investigated by isolating data points within the SO_2 plume, as detected using IASI SO_2 measurements. To identify regional depletion events, we computed the 5th percentile of ozone anomalies across all points within the SO_2 plume.

In contrast to UV-visible instruments, which reported significant perturbations in their ozone retrievals following the eruption (attributed to interference from SO_2 and H_2SO_4), no similar disturbances were observed in the IASI ozone retrievals. Because the spectral ranges used for ozone and SO_2 in the IASI retrieval algorithms do not overlap, results should not show any bias. Although sulfate aerosols may share some spectral range with ozone, the retrieval algorithm can effectively distinguish between the two, as sulfate aerosols exhibit strong absorption features and ozone variations are directly measured through its absorption lines. Thus, the IASI algorithm should account for ozone variability effectively following the Hunga eruption.

2.2 Aerosol measurements

In addition to the DIAL system, the OPAR is equipped with several other active remote sensing systems, including a Rayleigh-Mie lidar for aerosol profile measurements (Baron et al., 2023). In this study we used aerosol extinction profiles together with the corresponding stratospheric Aerosol Optical Depth (sAOD) at 532 nm as derived from the Rayleigh-Mie lidar measurements at the Reunion observatory. The data used in this study, which are publicly accessible via the Geosur website (https://geosur.osureunion.fr), are also available as a ready-to-use dataset from Baron (2023) (last accessed on 10 March 2025).

Aerosol optical properties can also be retrieved using sun-photometers. These remote sensing sun-tracking radiometers perform regular and frequent measurements of the direct solar spectral irradiance, typically at wavelengths between 340 and 1640 nm. By comparing the ground solar irradiance to the estimated top-of-the-atmosphere irradiance, they can determine the total AOD, a quantity that describes the opacity of the atmosphere to radiation. Therefore, a sun-photometer gives a measure of aerosol abundance in the atmospheric column above the study site. In the present study, we used AOD data from a Cimel sun-photometer located at the Saint-Denis campus, which has been operating since December 2003 in the framework of the AErosol

RObotic NETwork (AERONET) program. We used level 2.0 v3 AERONET data for the period from December 2003 to January 2022. AERONET data of level 2.0 is quality-controlled with near-real-time automatic cloud-screening in addition to having pre- and post-field calibrations. According to Giles et al. (2019), the 1σ uncertainty for the near-real-time AERONET AOD measurement is up to 0.02. The data are available from the AERONET website (https://aeronet.gsfc.nasa.gov/, last accessed on 10 March 2025).

The Ozone Mapping and Profiler Suite Limb Profiler (OMPS-LP) monitors the Earth limb ahead of its orbit path to provide high vertical resolution ozone and aerosol profiles. The instrument measures limb scattering radiances in the 290–1000 nm wavelength range over the sunlit portion of the atmosphere using three vertical slits. This instrument has been making observations onboard the Suomi National Polar-orbiting Partnership (Suomi NPP) spacecraft since January 2012, following a helio-synchronous orbit with an equatorial passing time of 13:30 solar time on its ascending node. With the goal to study the spatial extension of the plume, we used OMPS-LP aerosol extinction profiles at 745 nm. According to Taha et al. (2021), extinction coefficients at 745 nm have relative accuracy and precision of 10 % and 15 %, respectively. The OMPS data used in this study are available from the Goddard website (https://ozoneaq.gsfc.nasa.gov/, last accessed on 10 March 2025).

2.3 Trajectory model

To investigate the origin of the air masses in our study region, we used the HYbrid Single Particle Lagrangian Integrated Trajectory (HYSPLIT) model in its passive and backward mode (Draxler and Hess, 1997, 1998). Developed by the National Oceanic and Atmospheric Administration (NOAA), this model uses meteorological fields to compute trajectories of air masses. We used a single HYSPLIT simulation to track stratospheric air mass trajectories over the Indian Ocean. Thus, using meteorological fields from the Global Data Assimilation System (GDAS) (National Oceanic and Atmospheric Administration (NOAA), 2023), we ran a 240-hour back trajectory simulation of 12 distinct air parcels with terminal altitudes distributed equally between 23.5 and 29.0 km. These trajectories were chosen to have their endpoint at the location of Saint-Denis, Reunion. HYSPLIT trajectories can be obtained by running simulations via the HYSPLIT website (https://www.ready.noaa.gov/HYSPLIT_traj.php, last accessed on 10 March 2025).

2.4 Inter-comparison

Prior to drawing any conclusions based on the MLS ozone profiles, we compared them with Maïdo DIAL observations during background atmospheric conditions, representing a new contribution to the evaluation of MLS data in this region. For this inter-comparison process, we determined daily MLS ozone profiles by averaging all profiles within a 5-degree region around the lidar site. We averaged together MLS v5 ozone profiles from both the ascending and the descending sides of the Aura orbit, which have acquisition times near Reunion around 10:15 and 21:45 UTC, respectively. On the other hand, the 470 ground-based DIAL lidar profiles are only nocturnal (recorded at Reunion, i.e. approximately between 16:00 and 01:00 UTC, averaging around 18:30 UTC). Thus, the maximum temporal difference between MLS and lidar profiles is approximately 8 hours. Despite the non-overlapping acquisition times, we compared DIAL night profiles to daily MLS profiles. Although we obtained 470 DIAL profiles, the 5° inter-comparison radius limits the number of available MLS profiles, allowing inter-

comparison on a total of 340 days. Since lidar profiles use altitude as the vertical coordinate and MLS retrievals are output on

250 a pressure grid, we first converted the MLS pressure grid to an altitude grid using MLS geopotential height profiles. Following Sections 1.8 and 1.9 of Livesey et al. (2022), the comparison with lidar profiles was conducted by applying MLS averaging kernels and a priori ozone profiles, after reducing the resolution of the lidar profiles using least-squares smoothing. As a result, the profile comparison is based on the relative difference between the two datasets, as defined by the following formula:

$$\text{Relative}_{\text{bias}}(z) = 100 \times \frac{O_{3\;\text{MLS}}(z) - O_{3\;\text{DIAL}}(z)}{O_{3\;\text{DIAL}}(z)}, \tag{1}$$

255 where $O_{3\;\text{MLS}}(z)$ represents the MLS ozone value at an altitude z and $O_{3\;\text{DIAL}}(z)$ represents the smoothed stratospheric DIAL ozone value at the same altitude. Other statistical quantities were also determined, namely the number of profiles (N), the coefficient of correlation (r), the linear regression (in the form $y = ax$) and the Root-Mean-Square Deviation (RMSD). These statistical quantities were used to assess the differences and similarities between different ozone data in different layers.

Additionally, to compare IASI data with SAOZ measurements at Reunion under background atmospheric conditions, we

260 derived a daily TCO time series from Metop-B at Reunion, spanning March 2013 to December 2021. The inter-comparison utilized all data points from both datasets within this time period, irrespective of date and time of day, including all sunrise and sunset measurements.

3 Results and discussion

3.1 Aerosol plume

265 The Hunga main eruption occurred on 15 January 2022 and ejected a large quantity of H_2O and a moderate amount of SO_2 into the stratosphere (Khaykin et al., 2022; Sellitto et al., 2022; Zuo et al., 2022; Millán et al., 2022). Following the austral summer's general stratospheric circulation, the volcanic plume then traveled westward and reached the Indian Ocean and the African continent within days (Baron et al., 2023). The aerosol plume's transport across the Indian Ocean was captured by OMPS aerosol extinction profiles. Panel (a) of Fig. 1 shows the background aerosol distribution at 745 nm over the Indian

270 Ocean, captured prior to the arrival of the volcanic plume. Panels (b) to (e) present OMPS extinction coefficient profiles across different locations in the Indian Ocean as a function of latitude and altitude during the passage of the volcanic plume. At the bottom left of each panel are given the date and time of retrieval; the black dots correspond to the thermal tropopause estimated from the IASI temperature data using the WMO definition (WMO, 1957) and the vertical dashed lines mark the positions of the 5° S and 25° S latitude lines. Panel (f) traces the satellite tracks corresponding to data in panels (a) to (e). Thus,

275 this figure describes the latitudinal and vertical extent of the volcanic plume as observed by the satellite instrument during its passage over the Indian Ocean on 22 January, the date when impacts on ozone at Reunion were highest (Evan et al., 2023). During background atmospheric conditions (see Fig. 1a), the aerosol distribution shows that the largest values of the extinction coefficient are kept below the tropopause. Aerosol presence in the stratosphere is negligible compared to that in the troposphere. However, the presence of the volcanic plume becomes clearly visible on the other panels, where large extinction coefficient

values ($> 10^{-3}$) lie above the tropopause level and become comparable to those typically observed in the upper troposphere. On 22 January (Fig. 1b to 1e), the volcanic plume is clearly visible in the stratosphere over the Indian Ocean between 5° S and 25° S, reaching altitudes greater than 35 km. Note that this result only characterizes the vertical and latitudinal extent of the volcanic plume, but it does not describe the longitudinal dimension of the plume. Equivalent observations can also be obtained for 21 January (not shown). Similar results were found by Taha et al. (2022) as they outlined the presence of a volcanic plume located at an altitude exceeding 36 km. Additionally, they reported that the high sensitivity of OMPS LP enabled the monitoring of the volcanic plume at altitudes above 36 km for a duration of up to 90 days.

Figure 2 shows the Hunga aerosol plume as seen by two quasi-colocated instruments operating at the Maïdo observatory (lidar) and the Saint-Denis campus (sun-photometer). It is important to emphasize that the two instruments are 20 km apart with an approximately 2000 m difference in elevation. Even though the total AOD measured by the sun-photometer cannot be directly compared to the sAOD recorded by the lidar instrument, both sets of observations hold significant information about the passage of the volcanic plume. Figure 2a depicts the evolution of the lidar aerosol extinction profiles at 532 nm between 21 and 23 January, and Fig. 2b shows the evolution of the lidar sAOD at 532 nm (in black) and sun-photometer level 2.0 total AOD at 532 nm (in red) for the second half of January 2022. The lidar sAOD uncertainty is represented by the gray shading, while the sun-photometer AOD uncertainty, assumed to be about 0.02 (1σ) for all measurements (Giles et al., 2019), is illustrated in the upper part of the panel at the 2σ level. The sun-photometer AOD at 532 nm was obtained from the conversion of the AOD at 675 nm using the Angström exponent measurements between 440 and 675 nm. The blue line represents the multi-year average of sun-photometer level 2.0 AOD data for January, calculated from 2003 to 2021, with the shaded blue region indicating the corresponding standard deviation. Note that different horizontal axes are used for panels (a) and (b), and the common observation periods are enclosed by vertical dashed lines in the two panels.

Results in Fig. 2b show that the maximum total and stratospheric optical depths recorded by the two instruments in January 2022 are very high in comparison to the multi-year mean AOD of 0.05 ± 0.04. This is expected, as Reunion is a pristine region where January usually experiences low AOD levels (Duflot et al., 2022). After 20 January, total AOD values start to dramatically increase until 23 January, when they culminated at 0.57 ± 0.04 before gradually decreasing to return to background levels. Similar to the sun-photometer measurements, the Maïdo lidar reveals a large amount of aerosols after 21 January, with sAOD values rising up to 0.84 ± 0.27. A significant aerosol layer was seen by the lidar on two consecutive nights at altitudes of 29.7 km and 26.8 km, with maximum extinction coefficients of 0.53 ± 0.17 and 0.68 ± 0.11, respectively (see Fig. 2a). Note that sun-photometer measurements are obtained during the day, while lidar observations are only performed during nighttime. As such, observations from these two instruments cannot overlap as they do not operate simultaneously. A detailed study of the lidar observation of the Hunga plume can be found in Baron et al. (2023). Our results support their research, suggesting that the bulk of the Hunga aerosol plume passed over Reunion from 21 to 23 January.

3.2 Maïdo DIAL and MLS average ozone profiles

Figure 3 shows the average January Maïdo DIAL ozone profile, with the blue shaded area indicating the standard deviation. The orange and green lines represent the average January MLS ozone profiles representative of Reunion and the full study

region, respectively, with standard deviations shown as horizontal bars. The averages of all profiles remain within each other's standard deviation. Above 37 km, the average lidar profile slightly diverges from the average MLS profiles, likely due to decreased lidar SNR and fewer available profiles, which also increases the standard deviation. Still, average profiles are similar in the 15–37 km range. Because of the similarity between the lidar and MLS average ozone profiles over Reunion up to ∼30 km (the altitude of the higher Hunga cloud), MLS appears to be a suitable substitute for lidar data, as expected.

3.3 Inter-comparison results

Before analyzing ozone measurements and stratospheric transport, we conducted a statistical evaluation of differences between lidar and MLS observations, as well as between IASI and SAOZ data, under background atmospheric conditions. Specifically, we performed two comparisons: 1) MLS v5 ozone volume mixing ratio profiles over Reunion with Reunion's stratospheric DIAL ozone profiles from January 2013 to December 2021; and 2) SAOZ TCO with IASI TCO from March 2013 to December 2021.

Results are presented in Fig. 4, with panels (a) and (b) displaying the MLS/DIAL and IASI/SAOZ comparisons, respectively. The continuous line and the shaded area in Fig. 4a represent the mean relative bias computed from Eq. (1) and the standard error, respectively. This standard error represents the standard deviation divided by the square root of the number of individual comparisons (which varies as a function of altitude). The aforementioned statistical quantities are also shown in the figure. These mean relative bias profiles were obtained by averaging the relative bias values as derived from Eq. (1) across all available ozone profiles. Statistical results (correlation coefficient, linear regression and relative RMSD) presented in the following paragraphs were obtained from the comparison of all data points, irrespective of the altitude level, date and time of day.

Concerning ozone profiles, the best agreement is found in the 20–40 km altitude range, with larger biases and increasing deviations below 20 km and above 40 km. In the altitude range from 20 to 40 km, MLS has a relative bias and error (i.e. relative bias and error averaged over the 20–40 km altitude range, with respect to DIAL measurements) of 2.76 ± 1.40 %. In this altitude range, the standard error is low because of the large number of available comparison profiles (up to a maximum of 340). Between 40 and 45 km, the average relative bias decreases to -1.32 ± 4.80 %, whereas below 20 km, it shows an average of 10.81 ± 38.08 %. The increased relative bias and standard error at altitudes greater than 40 km is partly due to the lidar SNR decrease and the reduced number of lidar profiles reaching altitudes greater than 45 km. The decrease in SNR requires additional signal filtering, which introduces a high bias in the ozone lidar profile with respect to other measurements (Godin et al., 1999). Consequently, the lidar mean measurement error increases from ∼ 10 % at 40 km to ∼ 50 % at 47.5 km. Additionally, out of the 470 lidar profiles, 410 reached 40 km, 132 reached 45 km and only 6 reached 47.5 km. Note also that the increased relative bias and standard error at altitudes below 20 km may be due to the reduced satellite accuracy and precision at those levels (see Table 3.18.1 of Livesey et al. (2022)) and the smaller number of lidar profiles for these altitudes. Indeed, out of the 470 profiles, only 453 extend below 20 km, 409 below 17.5 km and 131 below 15 km. Over the whole altitude range, the correlation coefficient (r = 0.99) indicates an excellent correlation between the lidar and MLS, while the linear regression ($y = 1.02\,x$) and the mean relative bias profile show that MLS profiles tend to slightly over-estimate ozone

concentrations relative to DIAL, irrespective of the altitude. Finally, a moderate relative deviation (RMSD = 7.32 %) further demonstrates the agreement between MLS and the DIAL profiles.

Concerning TCO data, the large number of comparison points (N = 5619) enables precise statistics, indicating low relative deviation (RMSD = 3.26 %) and a fairly strong correlation (r = 0.87) between IASI and SAOZ datasets. The linear regression ($y = 1.02\,x$) shows that IASI TCO tends to slightly over-estimate SAOZ TCO.

Therefore, as expected, the MLS ozone profiles are in good agreement with lidar observations in the 20–40 km altitude range, including the altitudes of the Hunga-affected layers (25–30 km) that are our main focus in this study. The IASI and SAOZ TCO also exhibit low relative deviation and a high degree of correlation throughout the comparison period.

3.4 Effects of the volcanic plume on ozone

Based on the excellent correlation and agreement between satellite (MLS and IASI) and ground-based (stratospheric lidar and SAOZ) instruments over Reunion, we now use satellite ozone products to investigate the changes in the distribution of ozone over the study region.

Figure 5 depicts daily spatial distributions of SCO (panels (a1) to (a9)), SCO anomalies (panels (b1) to (b9)) and total SO_2 (panels (c1) to (c9)) over the Indian Ocean from 15 to 23 January. Similarly, Figure A1 in Appendix A provides the corresponding spatial distributions for TCO. Anomaly and SO_2 spatial distributions are overlaid with red contours of the SO_2 plume, indicating regions where the SO_2 total column is greater than 30 DU. SO_2 spatial distributions are complemented by the MLS satellite track (blue circles), with the MLS profiles meeting the Hunga-influenced selection criterion marked by dark blue circles. This selection criterion retains profiles if the v4 MLS H_2O mixing ratio exceeds 100 ppmv within the 10-100 hPa layer and if the the maximum occurs specifically at either 26.10 hPa ($\sim$25 km) or 14.68 hPa ($\sim$28 km), corresponding to the two Hunga-influenced layers. The successive locations of the SO_2 plume and the Hunga-influenced MLS profiles, which capture the H_2O and ozone anomalies, show the east-to-west displacement of Hunga-influenced air masses reported by previous studies (e.g. Millán et al. (2022); Khaykin et al. (2022); Baron et al. (2023)). The simultaneous displacement of the SO_2 and H_2O plumes supports previous studies, and the rapid disappearance of the high SO_2 anomaly indicates its conversion into sulfates under the influence of excess H_2O (Legras et al., 2022; Zhu et al., 2022, 2023; Asher et al., 2023).

This zonal movement is also reflected in the daily spatial distributions and anomalies of IASI TCO and SCO, suggesting a correlation between ozone, H_2O and SO_2 anomalies. The first significant negative ozone anomaly linked to Hunga appears on 15 January at 171° E, with values of -5.3 $\pm$ 4.7 DU for TCO and -16.4 $\pm$ 4.7 DU for SCO, where the uncertainty accounts for both the anomaly and column values from daily IASI observations. On this date, the 5th percentile of the anomaly is -10.0 DU for TCO and -6.2 DU for SCO. This first ozone anomaly is attributed to the lofting of ozone-poor tropospheric air masses (Zhu et al., 2023; Evan et al., 2023). The anomaly then appears to grow larger in size and amplitude as the SO_2 plume spreads, despite cloudy conditions on 18 January hindering IASI observations, before reaching Reunion on 21 January. The rapid conversion of SO_2 molecules to sulfate particles in the first days following the eruption increased the aerosol surface area, resulting in ozone depletion through heterogeneous chemistry (Zhu et al., 2023; Evan et al., 2023).

380 IASI recorded the highest number of negative ozone anomalies linked to Hunga on 20 and 21 January (panels (a6)-(a7) and (b6)-(b7) of Figs. 5 and A1). On 21 January, the 5th percentile of the anomaly peaked at -18.6 DU for TCO and at -14.5 DU for SCO. On the same day, extreme anomalies of -19.3 $\pm$ 5.0 DU for TCO and -32.8 $\pm$ 4.9 DU for SCO were observed at 71° E. At the same location, the IASI average SCO is 233.9 $\pm$ 9.4 DU, meaning this anomaly is more than three times larger than the typical variation. For TCO, the anomaly is about twice the climatological variability based on SAOZ data (262.8 $\pm$ 11.9

385 DU) and three times the variability derived from IASI's mean (258.9 $\pm$ 6.2 DU). The IASI anomaly spatial distributions for 20 and 21 January suggest the appearance of a large transient ozone depletion event extending over approximately 30 degrees of longitude and 20 degrees of latitude. The presence of clouds on 22 January hindered the retrieval of IASI data between Reunion and Madagascar, but large anomalies were still visible in the region on 23 January. The ozone anomaly then exited the Indian Ocean (not shown). Therefore, the anomaly spatial distributions and MLS satellite track indicate that the study region

390 was subject to TCO, SCO and H_2O anomalies over the latitudinal band from 30° S to 10° S, with a zonal westward shift of the ozone minimum. Similar to the findings of Evan et al. (2023), our results indicate the colocation of the H_2O and ozone anomalies as the Hunga plume passed over the Indian Ocean.

  MLS profiles identified by the criterion were studied further. Hunga-influenced profiles, defined as those with a water vapor mixing ratio exceeding 100 ppmv between 10 and 100 hPa, are categorized into two groups: those influenced by the higher-

395 altitude plume, with the highest water vapor mixing ratio at 14.68 hPa, and those influenced by the lower-altitude plume, with the maximum mixing ratio at 26.10 hPa. For each group of Hunga-influenced H_2O and ozone profiles, we computed the difference from their corresponding background average profiles. Subsequently, these individual differences were averaged, and results are presented in panels (a) and (b) of Fig. 6, where the horizontal bars represent the $\pm 1\sigma$ standard deviation around the mean value. Panels (c) and (d) present the same data on an altitude grid, with ozone anomaly profiles converted to partial

400 columns using geopotential and temperature information. These results show that, for each aerosol cloud with excess water vapor, the criterion leads to profiles with significant ozone loss at 1σ and water vapor excess at the same pressure ranges.

  The ozone mean anomaly associated with the higher-altitude cloud is (1σ) significant at the 12.11 hPa level and barely (1σ) significant at the 14.68 hPa pressure level, with an average anomaly of -0.7 $\pm$ 0.6 ppmv (-1.0 $\pm$ 1.0 DU/km) across these two pressure levels. In percentage terms, this corresponds to -5.5 $\pm$ 4.7 % and -6.3 $\pm$ 4.8 % with respect to the average MLS

405 profile over the Indian Ocean (Fig. 6e) and the mean lidar profile (Fig. 3), respectively. For the lower-altitude cloud, (1σ) significant ozone anomalies occur across the 21.54–31.62 hPa pressure range, with a mean anomaly of -0.6 $\pm$ 0.5 ppmv (-1.7 $\pm$ 1.4 DU/km), corresponding to -7.5 $\pm$ 7.0 % and -8.5 $\pm$ 8.1 % with respect to the mean MLS Indian Ocean and the mean lidar profiles, respectively. These results are consistent with those of Evan et al. (2023) who documented a 5 % depletion of stratospheric ozone over the Indian Ocean.

410 While Figs. 5 and A1 revealed local SCO and TCO minima, Fig. 6 shows clear reduction in stratospheric ozone (in the range 30–12 hPa, corresponding to 23.5–30.0 km) linked to sulfate aerosols and excess water vapor. This observation confirms previous research (Evan et al., 2023; Zhu et al., 2023) and indicates that the ozone anomaly arose from chemical loss.

3.5 Transport of air masses in the stratosphere

The Lagrangian HYSPLIT model was used to investigate the origin of the air masses responsible for the ozone anomaly over the Indian Ocean following the Hunga eruption. Back trajectories were run from the location of Reunion on 21 January at 00:00 for 12 distinct altitudes ranging between 23.5 and 29.0 km. Figure 7 shows the result of the HYSPLIT simulation with a color gradient to distinguish different air parcels. The orange trajectory represents air masses at 29.0 km altitude, and the black trajectory represents air masses at 23.5 km. Figure 7 shows that all back trajectories are zonal, moving westward and passing over the location of the Hunga eruption. The results of the HYSPLIT back trajectory simulation are consistent with the lidar measurements made in Reunion (see Fig. 2), as well as with the ozone anomalies over the region of study as depicted in Figs. A1 and 5. Additionally, these two figures also show a westward transition of ozone anomalies in the stratosphere over the Indian Ocean. The results of this trajectory simulation provide further confirmation of the Hunga plume's passage over Reunion, as previously established by Baron et al. (2023) and Evan et al. (2023).

4   Conclusions

The main eruption of the Hunga volcano released significant amounts of water vapor and a moderate quantity of sulfur dioxide into the atmosphere (Sellitto et al., 2022; Zuo et al., 2022; Millán et al., 2022), resulting in substantial anomalies within the stratosphere. Here we use satellite observations from IASI, MLS, and OMPS, complemented by ground-based measurements from Reunion, to provide a detailed view of the evolution of colocated ozone, water vapor, and SO_2 anomalies in the early volcanic plume over the Indian Ocean. This study presents the first analysis of IASI data in the context of Hunga.

OMPS aerosol extinction profiles revealed that the volcanic plume extended through the stratosphere, from 5° S to 25° S, and reached altitudes greater than 35 km over the Indian Ocean. These results are supported by the Maïdo aerosol lidar, which observed the plume during two consecutive nights, indicating that the core of the plume passed over Reunion at an altitude ranging from 26.8 to 29.7 km. Lidar sAOD and sun-photometer total AOD recorded unprecedented values of 0.84 ± 0.27 and 0.57 ± 0.04, respectively, during the passage of the plume.

The ozone anomaly associated with the volcanic plume was investigated using MLS and IASI ozone data. Based on these results, we state that the advection of the volcanic aerosol and water vapor plumes had an impact on stratospheric and total ozone abundances over the Indian Ocean. As indicated by IASI, a transient ozone depletion event was observed over the region, with the 5th percentile of the anomaly reaching -18.6 DU for Total Column Ozone (TCO) and -14.5 DU for Stratospheric Column Ozone (SCO) on 21 January. On the same day, extreme anomalies of -19.3 ± 5.0 DU for TCO and -32.8 ± 4.9 DU for SCO were observed, significantly exceeding climatological variability. Hunga-influenced MLS profiles show a significant reduction in ozone over the 30–12 hPa pressure range.

Ozone depletion occurred in two distinct layers, associated with two separate sulfate aerosol clouds with excess water vapor. Within the higher-altitude (14.68–12.12 hPa) cloud, ozone decreased by an average of 0.7 ± 0.6 ppmv (1.0 ± 1.0 DU/km). In percentage terms, this corresponds to -5.5 $\pm$ 4.7 % with respect to the average MLS profile over the Indian Ocean. Within the lower-altitude (31.62–21.54 hPa) cloud, ozone decreased by an average of 0.6 ± 0.5 ppmv (1.7 ± 1.4 DU/km), corresponding

to -7.5 $\pm$ 7.0 % with respect to the mean MLS Indian Ocean profile. Our findings refine previous reports of chemical ozone loss in the week following the eruption by showing that it was confined to two distinct aerosol layers with excess H_2O. This structured depletion offers new insight into the influence of Hunga aerosol distribution on ozone loss.

Appendix A: Appendix A

450 This section presents daily spatial distributions of TCO (panels (a1) to (a9)), TCO anomalies (panels (b1) to (b9)) and total SO_2 (panels (c1) to (c9)) over the Indian Ocean from 15 to 23 January.

Data availability. Reunion aerosol lidar data used in this study are accessible from https://doi.org/10.5281/zenodo.7790284 (last accessed on 10 March 2025). Reunion ozone lidar measurements are available through the NDACC page (https://ndacc.larc.nasa.gov/, last accessed on 10 March 2025). MLS data can be downloaded using NASA's data portal (https://disc.gsfc.nasa.gov/, last accessed on 10 March 2025).
455 IASI data are accessible from the AERIS website (https://iasi.aeris-data.fr, last accessed on 10 March 2025). SAOZ data can be downloaded from http://saoz.obs.uvsq.fr/ (last accessed on 10 March 2025). AERONET Version 3 Level 2 data are available from the AERONET website (https://aeronet.gsfc.nasa.gov/, last accessed on 10 March 2025). OMPS data can be accessed from the Goddard website (https://ozoneaq.gsfc.nasa.gov/, last accessed on 10 March 2025). HYSPLIT back trajectories can be obtained from the HYSPLIT website (https://www.ready.noaa.gov/HYSPLIT_traj.php, last accessed on 10 March 2025).

460 *Author contributions.* TM was the project leader; HB was the supervisor of the project; HB and NB participated in the methodology and interpretation of the results; all co-authors participated in the review of the manuscript.

Competing interests. The authors declare that they have no conflict of interest.

Acknowledgements. The authors acknowledge the CNRS-NRF IRP ARSAIO (Atmospheric Research in Southern Africa and Indian Ocean) project for supporting research activities, as well as the Conseil Régional de la Réunion for the Ph.D. scholarship of Tristan Millet. The
465 authors thank NASA for facilitating easy access and providing documentation for OMPS and MLS data. The authors extend their thanks to NOAA–ARL for supplying the HYSPLIT transport and dispersion model and to the Aeris data infrastructure (https://www.aeris-data.fr/) for providing access to the IASI Level 2 data used in this study. IASI is a joint mission of EUMETSAT and the Centre National d'Études Spatiales (CNES, France). The authors are appreciative of the PIs for providing data and their respective teams for maintaining the lidars and AERONET stations used in this study. The authors acknowledge the support of the European Commission through the REALISTIC project
470 (GA 101086690). This work was supported by the CNES, through the projects EECLAT, AOS and EXTRA-SAT. The project OBS4CLIM (Equipex project funded by ANR: ANR-21-ESRE-0013) is acknowledged. The authors acknowledge CNRS (INSU), Météo France, and Université de la Réunion for funding the OPAR infrastructure (Observatoire de Physique de l'Atmosphère à la Réunion) and OSU-R (Ob-

servatoires des Sciences de l'Univers à la Réunion, UAR 3365) for managing it. The Observatoire des Milieux Naturels et des Changements Globaux (OMNCG) federation of the OSU-R is also acknowledged. Lucien Froidevaux and Natalya Kramarova are warmly thanked for providing valuable insights into MLS and OMI data, respectively. The first author expresses heartfelt gratitude to Krzysztof Wargan for his significant contribution in providing valuable remarks that have improved the quality of the article. Finally, the authors warmly acknowledge the valuable contributions of the anonymous referees, whose detailed comments significantly enhanced the article's coherence and quality.

475

References

Aires, F., Rossow, W. B., Scott, N. A., and Chédin, A.: Remote sensing from the infrared atmospheric sounding interferometer instrument 2. Simultaneous retrieval of temperature, water vapor, and ozone atmospheric profiles, Journal of Geophysical Research: Atmospheres, 107, ACH 7–1–ACH 7–12, https://doi.org/https://doi.org/10.1029/2001JD001591, 2002.

Asher, E., Todt, M., Rosenlof, K., Thornberry, T., Gao, R.-S., Taha, G., Walter, P., Alvarez, S., Flynn, J., Davis, S. M., Evan, S., Brioude, J., Metzger, J.-M., Hurst, D. F., Hall, E., and Xiong, K.: Unexpectedly rapid aerosol formation in the Hunga Tonga plume, Proceedings of the National Academy of Sciences, 120, e2219547 120, https://doi.org/10.1073/pnas.2219547120, 2023.

Baray, J. L., Courcoux, Y., Keckhut, P., Portafaix, T., Tulet, P., Cammas, J. P., Hauchecorne, A., Godin Beekmann, S., De Mazière, M., Hermans, C., Desmet, F., Sellegri, K., Colomb, A., Ramonet, M., Sciare, J., Vuillemin, C., Hoareau, C., Dionisi, D., Duflot, V., Vérèmes, H., Porteneuve, J., Gabarrot, F., Gaudo, T., Metzger, J. M., Payen, G., Leclair de Bellevue, J., Barthe, C., Posny, F., Ricaud, P., Abchiche, A., and Delmas, R.: Maïdo observatory: a new high-altitude station facility at Reunion Island (21° S, 55° E) for long-term atmospheric remote sensing and in situ measurements, Atmospheric Measurement Techniques, 6, 2865–2877, https://doi.org/10.5194/amt-6-2865-2013, 2013.

Baron, A., Chazette, P., Khaykin, S., Payen, G., Marquestaut, N., Bègue, N., and Duflot, V.: Early Evolution of the Stratospheric Aerosol Plume Following the 2022 Hunga Tonga-Hunga Ha'apai Eruption: Lidar Observations From Reunion (21°S, 55°E), Geophysical Research Letters, 50, e2022GL101 751, https://doi.org/https://doi.org/10.1029/2022GL101751, e2022GL101751 2022GL101751, 2023.

Baron, A. A.: Early Evolution of the Stratospheric Aerosol Plume Following the 2022 Hunga Tonga-Hunga Ha'apai Eruption: Lidar Observations from Reunion Island (21°S, 55°E), https://doi.org/10.5281/zenodo.7790284, 2023.

Bernhard, G. H., Neale, R. E., Barnes, P. W., Neale, P. J., Zepp, R. G., Wilson, S. R., Andrady, A. L., Bais, A. F., McKenzie, R. L., Aucamp, P. J., Young, P. J., Liley, J. B., Lucas, R. M., Yazar, S., Rhodes, L. E., Byrne, S. N., Hollestein, L. M., Olsen, C. M., Young, A. R., Robson, T. M., Bornman, J. F., Jansen, M. A. K., Robinson, S. A., Ballaré, C. L., Williamson, C. E., Rose, K. C., Banaszak, A. T., Häder, D.-P., Hylander, S., Wängberg, S.-Å., Austin, A. T., Hou, W.-C., Paul, N. D., Madronich, S., Sulzberger, B., Solomon, K. R., Li, H., Schikowski, T., Longstreth, J., Pandey, K. K., Heikkilä, A. M., and White, C. C.: Environmental effects of stratospheric ozone depletion, UV radiation and interactions with climate change: UNEP Environmental Effects Assessment Panel, update 2019, Photochem. Photobiol. Sci., 19, 542–584, https://doi.org/10.1039/D0PP90011G, 2020.

Blumstein, D., Chalon, G., Carlier, T., Buil, C., Hebert, P., Maciaszek, T., Ponce, G., Phulpin, T., Tournier, B., Simeoni, D., Astruc, P., Clauss, A., Kayal, G., and Jegou, R.: IASI instrument: technical overview and measured performances, in: Infrared Space-borne Remote Sensing XII, edited by Strojnik, M., vol. 5543, pp. 196 – 207, International Society for Optics and Photonics, SPIE, https://doi.org/10.1117/12.560907, 2004.

Boynard, A., Hurtmans, D., Garane, K., Goutail, F., Hadji-Lazaro, J., Elissavet Koukouli, M., Wespes, C., Vigouroux, C., Keppens, A., Pommereau, J.-P., Pazmino, A., Balis, D., Loyola, D., Valks, P., Sussmann, R., Smale, D., Coheur, P.-F., and Clerbaux, C.: Validation of the IASI FORLI/EUMETSAT ozone products using satellite (GOME-2), ground-based (Brewer-Dobson, SAOZ, FTIR) and ozonesonde measurements, Atmospheric Measurement Techniques, 11, 5125–5152, https://doi.org/10.5194/amt-11-5125-2018, 2018.

Cadle, R. D., Fernald, F. G., and Frush, C. L.: Combined use of lidar and numerical diffusion models to estimate the quantity and dispersion of volcanic eruption clouds in the stratosphere: Vulcán Fuego, 1974, and Augustine, 1976, Journal of Geophysical Research (1896-1977), 82, 1783–1786, https://doi.org/https://doi.org/10.1029/JC082i012p01783, 1977.

Carr, J. L., Horváth, A., Wu, D. L., and Friberg, M. D.: Stereo Plume Height and Motion Retrievals for the Record-Setting Hunga Tonga-Hunga Ha'apai Eruption of 15 January 2022, Geophysical Research Letters, 49, e2022GL098 131, https://doi.org/https://doi.org/10.1029/2022GL098131, e2022GL098131 2022GL098131, 2022.

Clarisse, L., Hurtmans, D., Clerbaux, C., Hadji-Lazaro, J., Ngadi, Y., and Coheur, P.-F.: Retrieval of sulphur dioxide from the infrared atmospheric sounding interferometer (IASI), Atmospheric Measurement Techniques, 5, 581–594, https://doi.org/10.5194/amt-5-581-2012, 2012.

Clarisse, L., Coheur, P.-F., Theys, N., Hurtmans, D., and Clerbaux, C.: The 2011 Nabro eruption, a SO_2 plume height analysis using IASI measurements, Atmospheric Chemistry and Physics, 14, 3095–3111, https://doi.org/10.5194/acp-14-3095-2014, 2014.

Clerbaux, C., Boynard, A., Clarisse, L., George, M., Hadji-Lazaro, J., Herbin, H., Hurtmans, D., Pommier, M., Razavi, A., Turquety, S., Wespes, C., and Coheur, P.-F.: Monitoring of atmospheric composition using the thermal infrared IASI/MetOp sounder, Atmospheric Chemistry and Physics, 9, 6041–6054, https://doi.org/10.5194/acp-9-6041-2009, 2009.

Coheur, P.-F., Clarisse, L., Turquety, S., Hurtmans, D., and Clerbaux, C.: IASI measurements of reactive trace species in biomass burning plumes, Atmospheric Chemistry and Physics, 9, 5655–5667, https://doi.org/10.5194/acp-9-5655-2009, 2009.

Coy, L., Newman, P. A., Wargan, K., Partyka, G., Strahan, S. E., and Pawson, S.: Stratospheric Circulation Changes Associated With the Hunga Tonga-Hunga Ha'apai Eruption, Geophysical Research Letters, 49, e2022GL100 982, https://doi.org/https://doi.org/10.1029/2022GL100982, e2022GL100982 2022GL100982, 2022.

Crafford, T. C.: SO_2 emission of the 1974 eruption of Volcán Fuego, Guatemala, Bulletin Volcanologique, 39, 536–556, https://doi.org/10.1007/BF02596975, 1975.

Dhomse, S. S., Kinnison, D., Chipperfield, M. P., Salawitch, R. J., Cionni, I., Hegglin, M. I., Abraham, N. L., Akiyoshi, H., Archibald, A. T., Bednarz, E. M., Bekki, S., Braesicke, P., Butchart, N., Dameris, M., Deushi, M., Frith, S., Hardiman, S. C., Hassler, B., Horowitz, L. W., Hu, R.-M., Jöckel, P., Josse, B., Kirner, O., Kremser, S., Langematz, U., Lewis, J., Marchand, M., Lin, M., Mancini, E., Marécal, V., Michou, M., Morgenstern, O., O'Connor, F. M., Oman, L., Pitari, G., Plummer, D. A., Pyle, J. A., Revell, L. E., Rozanov, E., Schofield, R., Stenke, A., Stone, K., Sudo, K., Tilmes, S., Visioni, D., Yamashita, Y., and Zeng, G.: Estimates of ozone return dates from Chemistry-Climate Model Initiative simulations, Atmospheric Chemistry and Physics, 18, 8409–8438, https://doi.org/10.5194/acp-18-8409-2018, 2018.

Doiron, S. D., Bluth, G. J. S., Schnetzler, C. C., Krueger, A. J., and Walter, L. S.: Transport of Cerro Hudson SO2 clouds, Eos, Transactions American Geophysical Union, 72, 489–498, https://doi.org/https://doi.org/10.1029/90EO00354, 1991.

Draxler, R. and Hess, G.: Description of the HYSPLIT_4 modelling system, NOAA Tech. Mem. ERL ARL-224, 1997.

Draxler, R. and Hess, G.: An overview of the HYSPLIT_4 modelling system for trajectories, dispersion, and deposition, Australian Meteorological Magazine, 47, 295–308, 1998.

Duflot, V., Bègue, N., Pouliquen, M.-L., Goloub, P., and Metzger, J.-M.: Aerosols on the Tropical Island of La Réunion (21°S, 55°E): Assessment of Climatology, Origin of Variability and Trend, Remote Sensing, 14, 4945, https://doi.org/10.3390/rs14194945, 2022.

Evan, S., Brioude, J., Rosenlof, K. H., Gao, R.-S., Portmann, R. W., Zhu, Y., Volkamer, R., Lee, C. F., Metzger, J.-M., Lamy, K., Walter, P., Alvarez, S. L., Flynn, J. H., Asher, E., Todt, M., Davis, S. M., Thornberry, T., Vömel, H., Wienhold, F. G., Stauffer, R. M., Millán, L., Santee, M. L., Froidevaux, L., and Read, W. G.: Rapid ozone depletion after humidification of the stratosphere by the Hunga Tonga Eruption, Science, 382, eadg2551, https://doi.org/10.1126/science.adg2551, 2023.

Giles, D. M., Sinyuk, A., Sorokin, M. G., Schafer, J. S., Smirnov, A., Slutsker, I., Eck, T. F., Holben, B. N., Lewis, J. R., Campbell, J. R., Welton, E. J., Korkin, S. V., and Lyapustin, A. I.: Advancements in the Aerosol Robotic Network (AERONET) Version 3 database

– automated near-real-time quality control algorithm with improved cloud screening for Sun photometer aerosol optical depth (AOD) measurements, Atmospheric Measurement Techniques, 12, 169–209, https://doi.org/10.5194/amt-12-169-2019, 2019.

Gobbi, G. P., Congeduti, F., and Adriani, A.: Early stratospheric effects of the Pinatubo Eruption, Geophysical Research Letters, 19, 997–1000, https://doi.org/https://doi.org/10.1029/92GL01038, 1992.

Godin, S., Carswell, A. I., Donovan, D. P., Claude, H., Steinbrecht, W., McDermid, I. S., McGee, T. J., Gross, M. R., Nakane, H., Swart, D. P. J., Bergwerff, H. B., Uchino, O., von der Gathen, P., and Neuber, R.: Ozone differential absorption lidar algorithm intercomparison, Appl. Opt., 38, 6225–6236, https://doi.org/10.1364/AO.38.006225, 1999.

Godin-Beekmann, S., Porteneuve, J., and Garnier, A.: Systematic DIAL lidar monitoring of the stratospheric ozone vertical distribution at Observatoire de Haute-Provence (43.92 N, 5.71 E), Journal of environmental Monitoring, 5, 57–67, 2003.

Guo, S., Bluth, G. J. S., Rose, W. I., Watson, I. M., and Prata, A. J.: Re-evaluation of SO2 release of the 15 June 1991 Pinatubo eruption using ultraviolet and infrared satellite sensors, Geochemistry, Geophysics, Geosystems, 5, https://doi.org/https://doi.org/10.1029/2003GC000654, 2004.

Hofmann, D. J. and Oltmans, S. J.: Anomalous Antarctic ozone during 1992: Evidence for Pinatubo volcanic aerosol effects, Journal of Geophysical Research: Atmospheres, 98, 18 555–18 561, https://doi.org/https://doi.org/10.1029/93JD02092, 1993.

Hofmann, D. J. and Solomon, S.: Ozone destruction through heterogeneous chemistry following the eruption of El Chichón, Journal of Geophysical Research: Atmospheres, 94, 5029–5041, https://doi.org/https://doi.org/10.1029/JD094iD04p05029, 1989.

Hurtmans, D., Coheur, P.-F., Wespes, C., Clarisse, L., Scharf, O., Clerbaux, C., Hadji-Lazaro, J., George, M., and Turquety, S.: FORLI radiative transfer and retrieval code for IASI, Journal of Quantitative Spectroscopy and Radiative Transfer, 113, 1391–1408, https://doi.org/https://doi.org/10.1016/j.jqsrt.2012.02.036, three Leaders in Spectroscopy, 2012.

IPCC: Climate Change 2013: The Physical Science Basis. Contribution of Working Group I to the Fifth Assessment Report of the Intergovernmental Panel on Climate Change, in: Cambridge University Press, https://www.ipcc.ch/report/ar5/wg1/, 2013.

IPCC: Climate Change 2021: The Physical Science Basis. Contribution of Working Group I to the Sixth Assessment Report of the Intergovernmental Panel on Climate Change, in: Cambridge University Press, https://www.ipcc.ch/report/ar6/wg1/, 2021.

Ivatt, P. D., Evans, M. J., and Lewis, A. C.: Suppression of surface ozone by an aerosol-inhibited photochemical ozone regime, Nature Geoscience, 15, 536–540, https://doi.org/10.1038/s41561-022-00972-9, 2022.

Ivy, D. J., Solomon, S., Kinnison, D., Mills, M. J., Schmidt, A., and Neely III, R. R.: The influence of the Calbuco eruption on the 2015 Antarctic ozone hole in a fully coupled chemistry-climate model, Geophysical Research Letters, 44, 2556–2561, https://doi.org/https://doi.org/10.1002/2016GL071925, 2017.

Jacob, D. J.: Introduction to atmospheric chemistry, Princeton University Press, 1999.

Khaykin, S., Podglajen, A., Ploeger, F., Grooß, J.-U., Tence, F., Bekki, S., Khlopenkov, K., Bedka, K., Rieger, L., Baron, A., Godin-Beekmann, S., Legras, B., Sellitto, P., Sakai, T., Barnes, J., Uchino, O., Morino, I., Nagai, T., Wing, R., Baumgarten, G., Gerding, M., Duflot, V., Payen, G., Jumelet, J., Querel, R., Liley, B., Bourassa, A., Clouser, B., Feofilov, A., Hauchecorne, A., and Ravetta, F.: Global perturbation of stratospheric water and aerosol burden by Hunga eruption, Communications Earth & Environment, 3, 316, https://doi.org/10.1038/s43247-022-00652-x, 2022.

Kirchner, I., Stenchikov, G. L., Graf, H.-F., Robock, A., and Antuña, J. C.: Climate model simulation of winter warming and summer cooling following the 1991 Mount Pinatubo volcanic eruption, Journal of Geophysical Research: Atmospheres, 104, 19 039–19 055, https://doi.org/https://doi.org/10.1029/1999JD900213, 1999.

Kremser, S., Thomason, L. W., von Hobe, M., Hermann, M., Deshler, T., Timmreck, C., Toohey, M., Stenke, A., Schwarz, J. P., Weigel, R., Fueglistaler, S., Prata, F. J., Vernier, J.-P., Schlager, H., Barnes, J. E., Antuña-Marrero, J.-C., Fairlie, D., Palm, M., Mahieu, E., Notholt, J., Rex, M., Bingen, C., Vanhellemont, F., Bourassa, A., Plane, J. M. C., Klocke, D., Carn, S. A., Clarisse, L., Trickl, T., Neely, R., James, A. D., Rieger, L., Wilson, J. C., and Meland, B.: Stratospheric aerosol—Observations, processes, and impact on climate, Reviews of Geophysics, 54, 278–335, https://doi.org/https://doi.org/10.1002/2015RG000511, 2016.

Legras, B., Duchamp, C., Sellitto, P., Podglajen, A., Carboni, E., Siddans, R., Grooß, J.-U., Khaykin, S., and Ploeger, F.: The evolution and dynamics of the Hunga Tonga–Hunga Ha'apai sulfate aerosol plume in the stratosphere, Atmospheric Chemistry and Physics, 22, 14 957–14 970, https://doi.org/10.5194/acp-22-14957-2022, 2022.

Livesey, N. J., Read, W. G., Wagner, P. A., Froidevaux, L., Lambert, A., Manney, G. L., Valle, L. F. M., Pumphrey, H. C., Santee, M. L., Schwartz, M. J., Wang, S., Fuller, R. A., Jarnot, R. F., Knosp, B. W., Martinez, E., and Lay, R. R.: Version 4.2x Level 2 and 3 data quality and description document., https://mls.jpl.nasa.gov/data/v4-2_data_quality_document.pdf, 2020.

Livesey, N. J., Read, W. G., Wagner, P. A., Froidevaux, L., Santee, M. L., Schwartz, M. J., Lambert, A., Valle, L. F. M., Pumphrey, H. C., Manney, G. L., Fuller, R. A., Jarnot, R. F., Knosp, B. W., and Lay, R. R.: Version 5.0x Level 2 and 3 data quality and description document., https://mls.jpl.nasa.gov/data/v5-0_data_quality_document.pdf, 2022.

Matsumura, Y. and Ananthaswamy, H. N.: Toxic effects of ultraviolet radiation on the skin, Toxicology and Applied Pharmacology, 195, 298–308, https://doi.org/https://doi.org/10.1016/j.taap.2003.08.019, toxicology of the Skin, 2004.

McCormick, M., Thomason, L., and Trepte, C.: Atmospheric effects of the Mt Pinatubo eruption, Nature, 373, 399–404, https://www.nature.com/articles/373399a0, 1995.

Mills, G., Sharps, K., Simpson, D., Pleijel, H., Frei, M., Burkey, K., Emberson, L., Uddling, J., Broberg, M., Feng, Z., Kobayashi, K., and Agrawal, M.: Closing the global ozone yield gap: Quantification and cobenefits for multistress tolerance, Global Change Biology, 24, 4869–4893, https://doi.org/https://doi.org/10.1111/gcb.14381, 2018.

Millán, L., Santee, M. L., Lambert, A., Livesey, N. J., Werner, F., Schwartz, M. J., Pumphrey, H. C., Manney, G. L., Wang, Y., Su, H., Wu, L., Read, W. G., and Froidevaux, L.: The Hunga Tonga-Hunga Ha'apai Hydration of the Stratosphere, Geophysical Research Letters, 49, e2022GL099 381, https://doi.org/https://doi.org/10.1029/2022GL099381, e2022GL099381 2022GL099381, 2022.

Molina, M. J. and Rowland, F. S.: Stratospheric sink for chlorofluoromethanes: chlorine atom-catalysed destruction of ozone, Nature, 249, 810–812, https://doi.org/10.1038/249810a0, 1974.

National Oceanic and Atmospheric Administration (NOAA): Global Data Assimilation System (GDAS), https://www.ready.noaa.gov/data/archives/gdas1/, accessed September 2022, 2023.

Neale, R. E., Barnes, P. W., Robson, T. M., Neale, P. J., Williamson, C. E., Zepp, R. G., Wilson, S. R., Madronich, S., Andrady, A. L., Heikkilä, A. M., Bernhard, G. H., Bais, A. F., Aucamp, P. J., Banaszak, A. T., Bornman, J. F., Bruckman, L. S., Byrne, S. N., Foereid, B., Häder, D.-P., Hollestein, L. M., Hou, W.-C., Hylander, S., Jansen, M. A. K., Klekociuk, A. R., Liley, J. B., Longstreth, J., Lucas, R. M., Martinez-Abaigar, J., McNeill, K., Olsen, C. M., Pandey, K. K., Rhodes, L. E., Robinson, S. A., Rose, K. C., Schikowski, T., Solomon, K. R., Sulzberger, B., Ukpebor, J. E., Wang, Q.-W., Wängberg, S.-Å., White, C. C., Yazar, S., Young, A. R., Young, P. J., Zhu, L., and Zhu, M.: Environmental effects of stratospheric ozone depletion, UV radiation, and interactions with climate change: UNEP Environmental Effects Assessment Panel, Update 2020, Photochemical & Photobiological Sciences, 20, 1–67, https://doi.org/10.1007/s43630-020-00001-x, 2021.

Nuvolone, D., Petri, D., and Voller, F.: The Effects of Ozone on Human Health, Environmental Science and Pollution Research, 25, 8074–8088, https://doi.org/10.1007/s11356-017-9239-3, 2018.

Orphal, J., Staehelin, J., Tamminen, J., Braathen, G., De Backer, M.-R., Bais, A., Balis, D., Barbe, A., Bhartia, P. K., Birk, M., Burkholder, J. B., Chance, K., von Clarmann, T., Cox, A., Degenstein, D., Evans, R., Flaud, J.-M., Flittner, D., Godin-Beekmann, S., Gorshelev, V., Gratien, A., Hare, E., Janssen, C., Kyrölä, E., McElroy, T., McPeters, R., Pastel, M., Petersen, M., Petropavlovskikh, I., Picquet-Varrault, B., Pitts, M., Labow, G., Rotger-Languereau, M., Leblanc, T., Lerot, C., Liu, X., Moussay, P., Redondas, A., Van Roozendael, M., Sander, S. P., Schneider, M., Serdyuchenko, A., Veefkind, P., Viallon, J., Viatte, C., Wagner, G., Weber, M., Wielgosz, R. I., and Zehner, C.: Absorption cross-sections of ozone in the ultraviolet and visible spectral regions: Status report 2015, Journal of Molecular Spectroscopy, 327, 105–121, https://doi.org/https://doi.org/10.1016/j.jms.2016.07.007, new Visions of Spectroscopic Databases, Volume II, 2016.

Pazmiño, A.: DIAL lidar for ozone measurements, in: Journal de Physique IV (Proceedings), vol. 139, pp. 361–372, EDP sciences, 2006.

Pitts, D. G., Cullen, A. P., and Hacker, P. D.: Ocular effects of ultraviolet radiation from 295 to 365 nm., Investigative Ophthalmology & Visual Science, 16, 932–939, 1977.

Pommereau, J. P. and Goutail, F.: O_3 and NO_2 ground-based measurements by visible spectrometry during Arctic winter and spring 1988, Geophysical Research Letters, 15, 891–894, https://doi.org/10.1029/GL015i008p00891, 1988.

Portafaix, T., Godin-Beekmann, S., Payen, G., Langerock, B., Fernandez, S., Posny, F., Cammas, J.-P., Metzger, J.-M., Bencherif, H., Vigouroux, C., and Marquestaut, N.: Ozone profiles obtained by DIAL technique at Maïdo Observatory in La Réunion Island: comparisons with ECC ozone-sondes, ground-based FTIR spectrometer and microwave radiometer measurements, EPJ Web of Conferences, 119, https://doi.org/10.1051/epjconf/201611905005, 2015.

Ramaswamy, V., Schwarzkopf, M. D., Randel, W. J., Santer, B. D., Soden, B. J., and Stenchikov, G. L.: Anthropogenic and Natural Influences in the Evolution of Lower Stratospheric Cooling, Science, 311, 1138–1141, https://doi.org/10.1126/science.1122587, 2006.

Robock, A.: Volcanic eruptions and climate, Reviews of Geophysics, 38, 191–219, https://doi.org/https://doi.org/10.1029/1998RG000054, 2000.

Rowland, F. S.: Stratospheric ozone depletion by chlorofluorocarbons (Nobel lecture), Angewandte Chemie International Edition in English, 35, 1786–1798, 1996.

Santee, M. L., Lambert, A., Froidevaux, L., Manney, G. L., Schwartz, M. J., Millán, L. F., Livesey, N. J., Read, W. G., Werner, F., and Fuller, R. A.: Strong Evidence of Heterogeneous Processing on Stratospheric Sulfate Aerosol in the Extrapolar Southern Hemisphere Following the 2022 Hunga Tonga-Hunga Ha'apai Eruption, Journal of Geophysical Research: Atmospheres, 128, e2023JD039 169, https://doi.org/https://doi.org/10.1029/2023JD039169, e2023JD039169 2023JD039169, 2023.

Schoeberl, M. R., Doiron, S. D., Lait, L. R., Newman, P. A., and Krueger, A. J.: A simulation of the Cerro Hudson SO2 cloud, Journal of Geophysical Research: Atmospheres, 98, 2949–2955, https://doi.org/https://doi.org/10.1029/92JD02517, 1993.

Schoeberl, M. R., Wang, Y., Ueyama, R., Taha, G., Jensen, E., and Yu, W.: Analysis and Impact of the Hunga Tonga-Hunga Ha'apai Stratospheric Water Vapor Plume, Geophysical Research Letters, 49, e2022GL100 248, https://doi.org/https://doi.org/10.1029/2022GL100248, e2022GL100248 2022GL100248, 2022.

Sellitto, P., Podglajen, A., Belhadji, R., Boichu, M., Carboni, E., Cuesta, J., Duchamp, C., Kloss, C., Siddans, R., Bègue, N., Blarel, L., Jegou, F., Khaykin, S., Renard, J.-B., and Legras, B.: The unexpected radiative impact of the Hunga Tonga eruption of 15th January 2022, Communications Earth & Environment, 3, 288, https://doi.org/10.1038/s43247-022-00618-z, 2022.

Sicard, M., Baron, A., Ranaivombola, M., Gantois, D., Millet, T., Sellitto, P., Bègue, N., Bencherif, H., Payen, G., Marquestaut, N., and Duflot, V.: Radiative impact of the Hunga stratospheric volcanic plume: role of aerosols and water vapor over Réunion Island ($21°$ S, $55°$ E), Atmospheric Chemistry and Physics, 25, 367–381, https://doi.org/10.5194/acp-25-367-2025, 2025.

Solomon, S.: The mystery of the Antarctic ozone "hole", Reviews of Geophysics, 26, 131–148, 1988.

665 Solomon, S.: Stratospheric ozone depletion: A review of concepts and history, Reviews of Geophysics, 37, 275–316, https://doi.org/https://doi.org/10.1029/1999RG900008, 1999.

Stenchikov, G. L., Kirchner, I., Robock, A., Graf, H.-F., Antuña, J. C., Grainger, R. G., Lambert, A., and Thomason, L.: Radiative forcing from the 1991 Mount Pinatubo volcanic eruption, Journal of Geophysical Research: Atmospheres, 103, 13 837–13 857, https://doi.org/https://doi.org/10.1029/98JD00693, 1998.

670 Taha, G., Loughman, R., Zhu, T., Thomason, L., Kar, J., Rieger, L., and Bourassa, A.: OMPS LP Version 2.0 multi-wavelength aerosol extinction coefficient retrieval algorithm, Atmospheric Measurement Techniques, 14, 1015–1036, https://doi.org/10.5194/amt-14-1015-2021, 2021.

Taha, G., Loughman, R., Colarco, P. R., Zhu, T., Thomason, L. W., and Jaross, G.: Tracking the 2022 Hunga Tonga-Hunga Ha'apai Aerosol Cloud in the Upper and Middle Stratosphere Using Space-Based Observations, Geophysical Research Letters, 49, e2022GL100 091,
675 https://doi.org/https://doi.org/10.1029/2022GL100091, e2022GL100091 2022GL100091, 2022.

Tie, X. and Brasseur, G.: The response of stratospheric ozone to volcanic eruptions: Sensitivity to atmospheric chlorine loading, Geophysical Research Letters, 22, 3035–3038, https://doi.org/https://doi.org/10.1029/95GL03057, 1995.

Vömel, H., Evan, S., and Tully, M.: Water vapor injection into the stratosphere by Hunga Tonga-Hunga Ha'apai, Science, 377, 1444–1447, https://doi.org/10.1126/science.abq2299, 2022.

680 Waters, J., Froidevaux, L., Harwood, R., Jarnot, R., Pickett, H., Read, W., Siegel, P., Cofield, R., Filipiak, M., Flower, D., Holden, J., Lau, G., Livesey, N., Manney, G., Pumphrey, H., Santee, M., Wu, D., Cuddy, D., Lay, R., Loo, M., Perun, V., Schwartz, M., Stek, P., Thurstans, R., Boyles, M., Chandra, K., Chavez, M., Chen, G.-S., Chudasama, B., Dodge, R., Fuller, R., Girard, M., Jiang, J., Jiang, Y., Knosp, B., LaBelle, R., Lam, J., Lee, K., Miller, D., Oswald, J., Patel, N., Pukala, D., Quintero, O., Scaff, D., Van Snyder, W., Tope, M., Wagner, P., and Walch, M.: The Earth Observing System Microwave Limb Sounder (EOS MLS) on the Aura Satellite, IEEE Transactions on
685 Geoscience and Remote Sensing, 44, 1075–1092, https://doi.org/10.1109/TGRS.2006.873771, 2006.

Wilmouth, D. M., Østerstrøm, F. F., Smith, J. B., Anderson, J. G., and Salawitch, R. J.: Impact of the Hunga Tonga volcanic eruption on stratospheric composition, Proceedings of the National Academy of Sciences, 120, e2301994 120, https://doi.org/10.1073/pnas.2301994120, 2023.

WMO: Definition of the tropopause, Tech. rep., World Meteorological Organization, 1957.

690 WMO: Scientific assessment of ozone depletion: 1998, Global ozone research and monitoring project-report no. 44, World Meteorological Organization, Geneva, Switzerland, https://library.wmo.int/idurl/4/50254, 1999.

WMO: Scientific assessment of ozone depletion: 2022, Gaw report no. 278, World Meteorological Organization, Geneva, Switzerland, https://library.wmo.int/idurl/4/58360, 2022.

Wright, C. J., Hindley, N. P., Alexander, M. J., Barlow, M., Hoffmann, L., Mitchell, C. N., Prata, F., Bouillon, M., Carstens, J., Clerbaux, C.,
695 Osprey, S. M., Powell, N., Randall, C. E., and Yue, J.: Surface-to-space atmospheric waves from Hunga Tonga–Hunga Ha'apai eruption, Nature, 609, 741–746, https://doi.org/10.1038/s41586-022-05012-5, 2022.

Yook, S., Thompson, D. W. J., and Solomon, S.: Climate Impacts and Potential Drivers of the Unprecedented Antarctic Ozone Holes of 2020 and 2021, Geophysical Research Letters, 49, e2022GL098 064, https://doi.org/https://doi.org/10.1029/2022GL098064, e2022GL098064 2022GL098064, 2022.

700 Zhang, J., Wang, P., Kinnison, D., Solomon, S., Guan, J., Stone, K., and Zhu, Y.: Stratospheric Chlorine Processing After the Unprecedented Hunga Tonga Eruption, Geophysical Research Letters, 51, e2024GL108 649, https://doi.org/https://doi.org/10.1029/2024GL108649, e2024GL108649 2024GL108649, 2024.

Zhu, Y., Toon, O. B., Kinnison, D., Harvey, V. L., Mills, M. J., Bardeen, C. G., Pitts, M., Bègue, N., Renard, J.-B., Berthet, G., and Jégou, F.: Stratospheric Aerosols, Polar Stratospheric Clouds, and Polar Ozone Depletion After the Mount Calbuco Eruption in 2015, Journal of Geophysical Research: Atmospheres, 123, 12,308–12,331, https://doi.org/https://doi.org/10.1029/2018JD028974, 2018.

Zhu, Y., Bardeen, C. G., Tilmes, S., Mills, M. J., Wang, X., Harvey, V. L., Taha, G., Kinnison, D., Portmann, R. W., Yu, P., Rosenlof, K. H., Avery, M., Kloss, C., Li, C., Glanville, A. S., Millán, L., Deshler, T., Krotkov, N., and Toon, O. B.: Perturbations in stratospheric aerosol evolution due to the water-rich plume of the 2022 Hunga-Tonga eruption, Communications Earth & Environment, 3, 248, https://doi.org/10.1038/s43247-022-00580-w, 2022.

Zhu, Y., Portmann, R. W., Kinnison, D., Toon, O. B., Millán, L., Zhang, J., Vömel, H., Tilmes, S., Bardeen, C. G., Wang, X., Evan, S., Randel, W. J., and Rosenlof, K. H.: Stratospheric ozone depletion inside the volcanic plume shortly after the 2022 Hunga Tonga eruption, Atmospheric Chemistry and Physics, 23, 13 355–13 367, https://doi.org/10.5194/acp-23-13355-2023, 2023.

Zuo, M., Zhou, T., Man, W., Chen, X., Liu, J., Liu, F., and Gao, C.: Volcanoes and Climate: Sizing up the Impact of the Recent Hunga Tonga-Hunga Ha'apai Volcanic Eruption from a Historical Perspective, Advances in Atmospheric Sciences, https://doi.org/10.1007/s00376-022-2034-1, 2022.
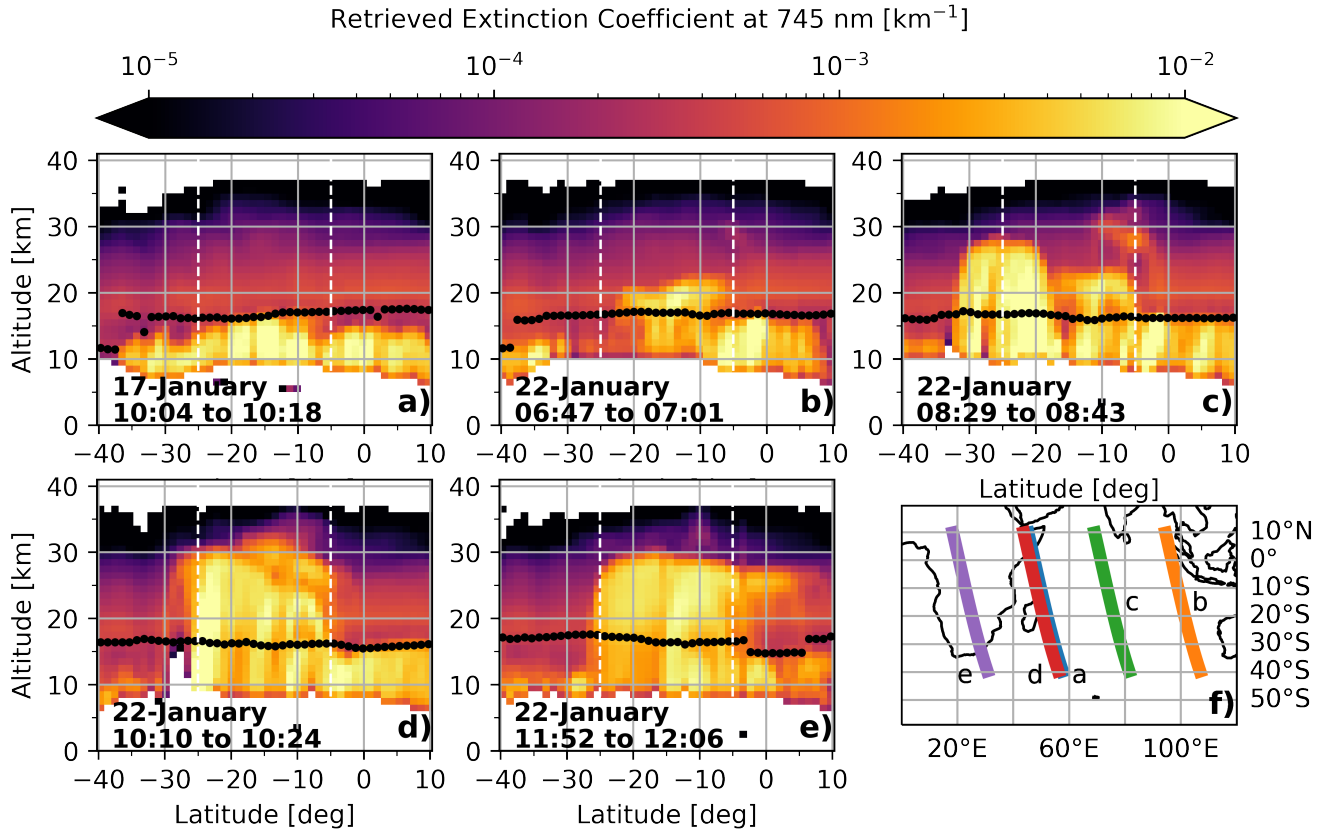
Figure 1. OMPS-LP aerosol extinction height-latitude cross-sections over the Indian Ocean at 745 nm for (**a**) background conditions on 17 January prior to the passage of the volcanic plume and (**b–e**) during the passage of the plume on 22 January. Panel (**f**) shows the satellite track corresponding to each overpass. The superimposed black dots on panels (**a–e**) indicate the tropopause altitude estimated from the IASI temperature data, using the WMO definition (WMO, 1957). Vertical dashed lines mark the positions of the 5° S and 25° S latitude lines.
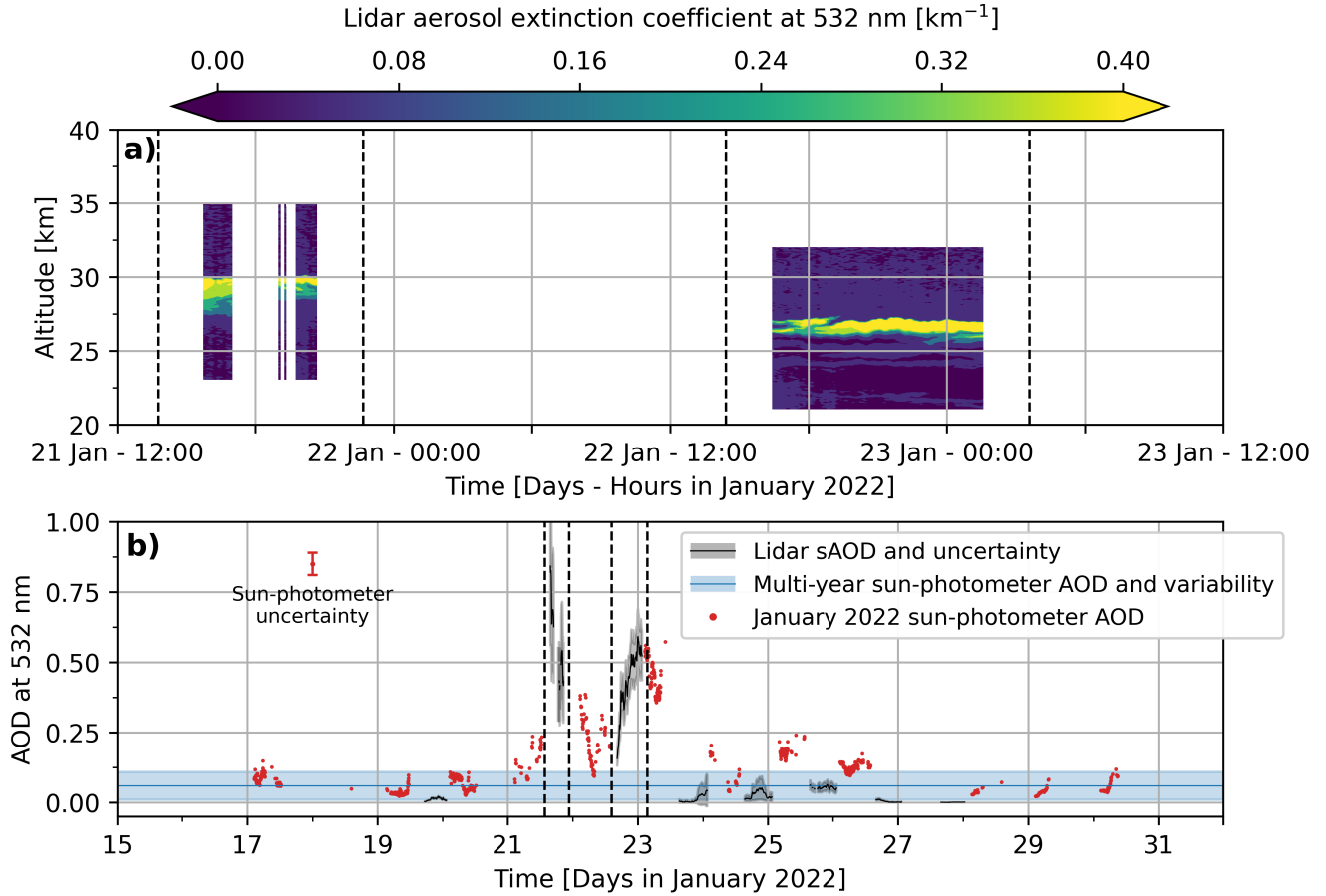
Figure 2. (**a**) Aerosol lidar extinction profiles at 532 nm and (**b**) aerosol lidar stratospheric AOD (sAOD) in black with level 2.0 sun-photometer total AOD in red. The gray shading indicates the lidar sAOD uncertainty, while the sun-photometer total AOD uncertainty is illustrated in the upper part of panel (**b**). The blue line and shaded area represent average and standard deviation values given by level 2.0 sun-photometer data from the months of January taken between 2003 and 2021. The common observation periods in the two panels are visually represented with vertical dashed lines.
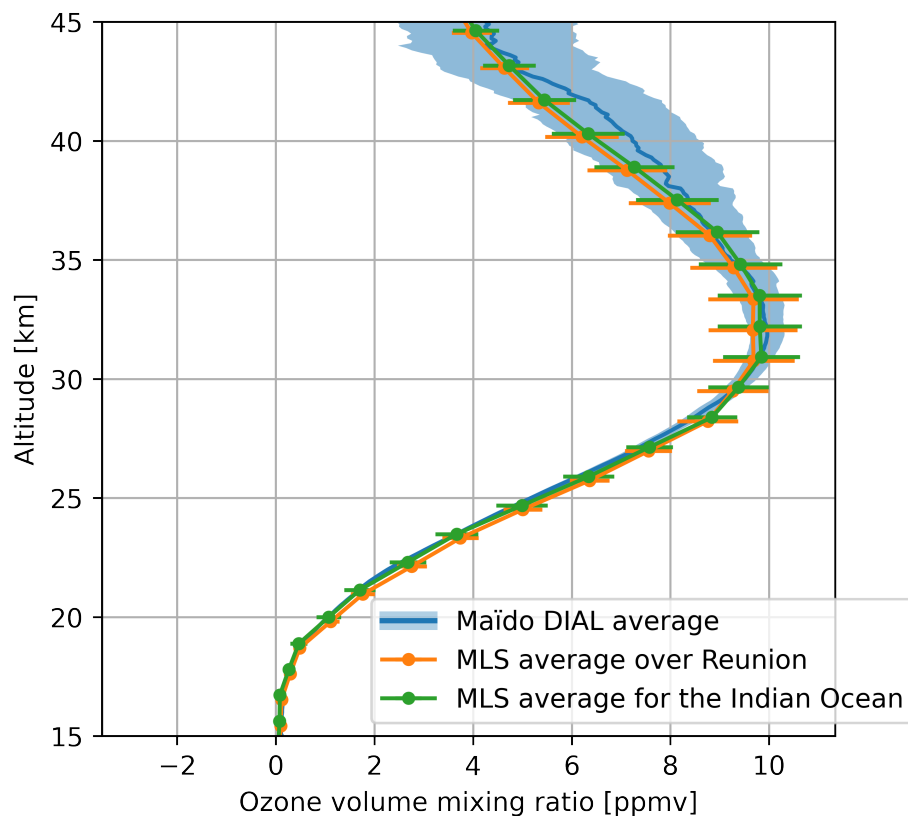
Figure 3. Average January stratospheric DIAL profile calculated from observations taken over 2013—2021 at Reunion (blue), alongside average January MLS profiles for Reunion (orange) and the full study region (green). Standard deviations are shown as a shaded region for the DIAL profile and as horizontal bars for the MLS profiles.
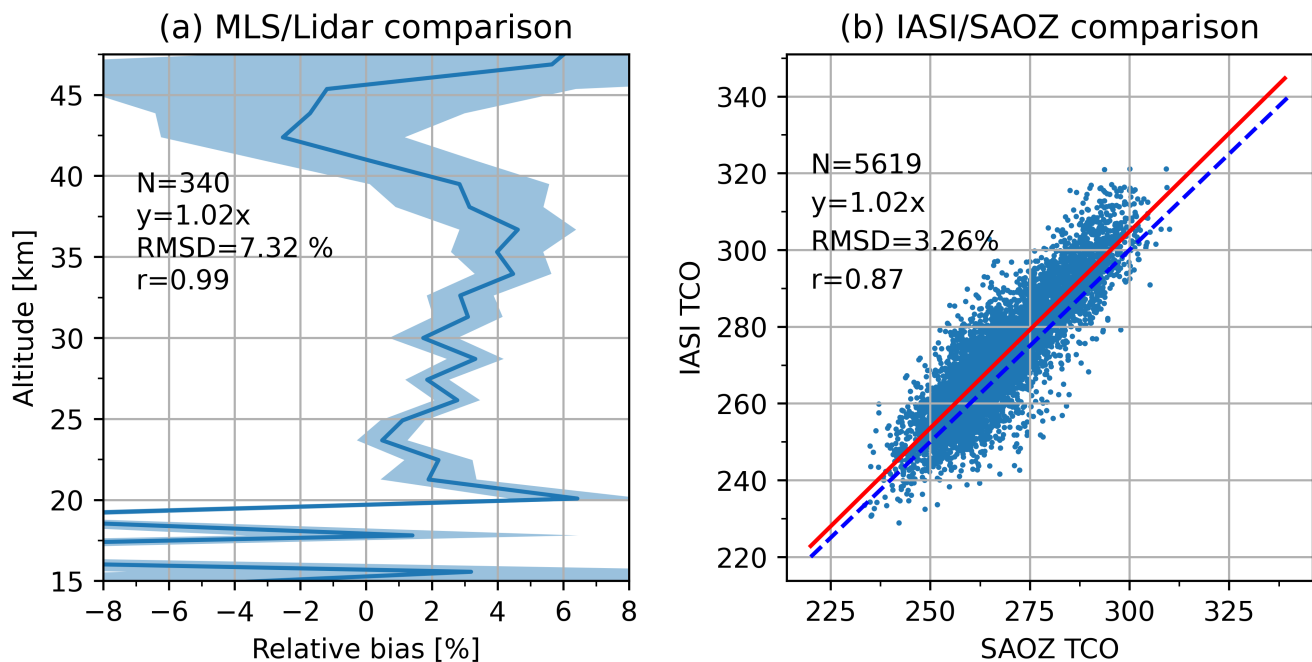
Figure 4. (**a**) Mean relative bias (solid line) and standard error (shaded area) computed from Eq. (1) comparing nocturnal DIAL ozone profiles to the corresponding daily MLS v5 ozone profiles between January 2013 and December 2021. (**b**) Direct comparison between SAOZ Total Column Ozone (TCO) and IASI TCO from data points obtained between March 2013 and December 2021. The solid red and dashed blue lines represent the linear regression line and the 1:1 line, respectively. Statistical results presented in the left side each of panel were obtained from the comparison of all data points, irrespective of the altitude level, date and time of day.
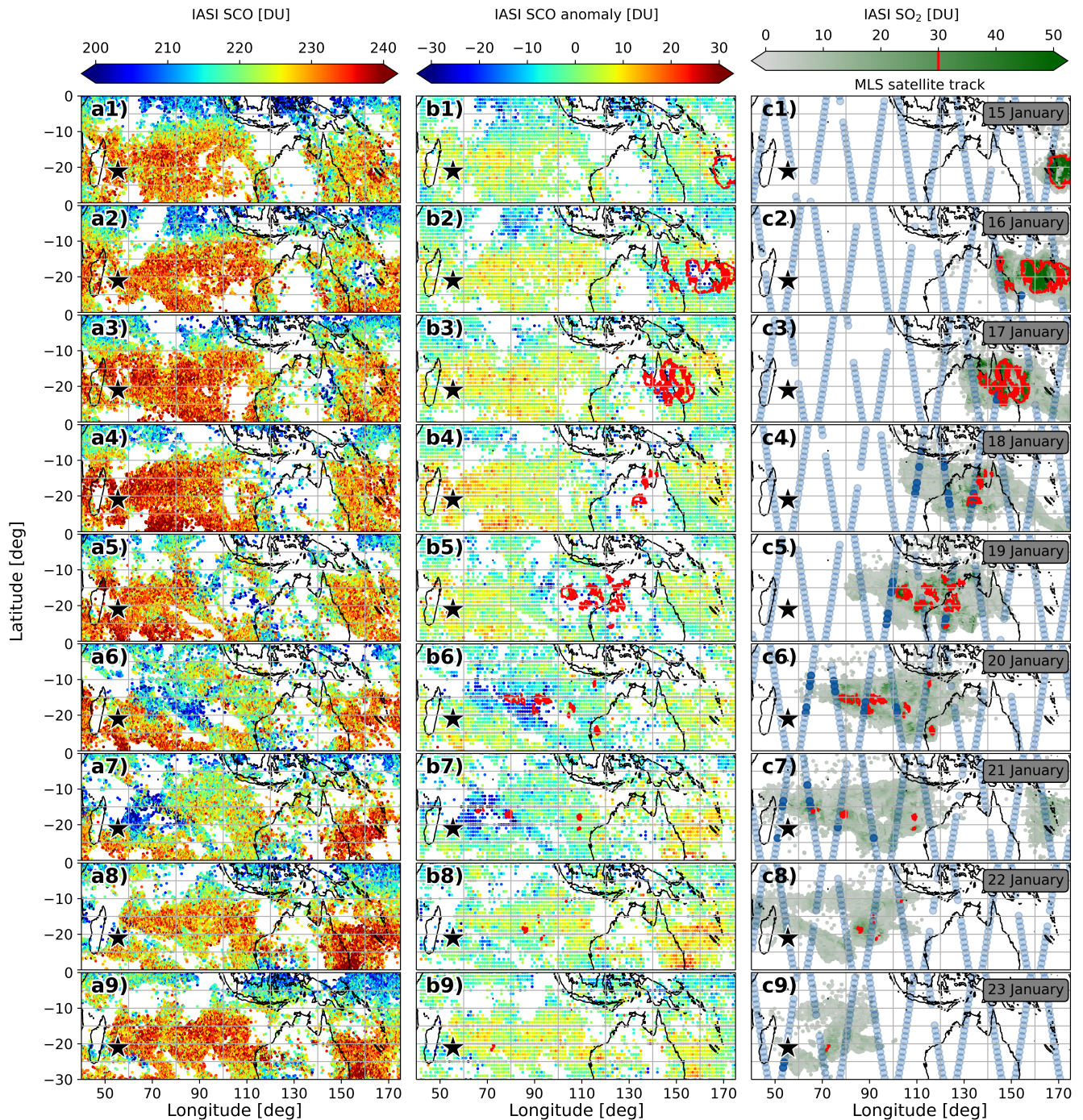
Figure 5. Daily evolution of (**a1-a9**) Stratospheric Column Ozone (SCO) and (**b1-b9**) SCO anomaly observed by IASI alongside (**c1-c9**) the satellite track of MLS (blue dots) and total SO_2 column from IASI between 15 and 23 January 2022. Dark blue dots on the MLS track represent the location of profiles meeting the Hunga-influenced selection criterion. The red contour indicates the regions where total SO_2 column is greater than 30 DU. The black and white star represents the location of Reunion. Each row corresponds to a distinct day, and the date of observation is indicated for each row in the right column. **28**
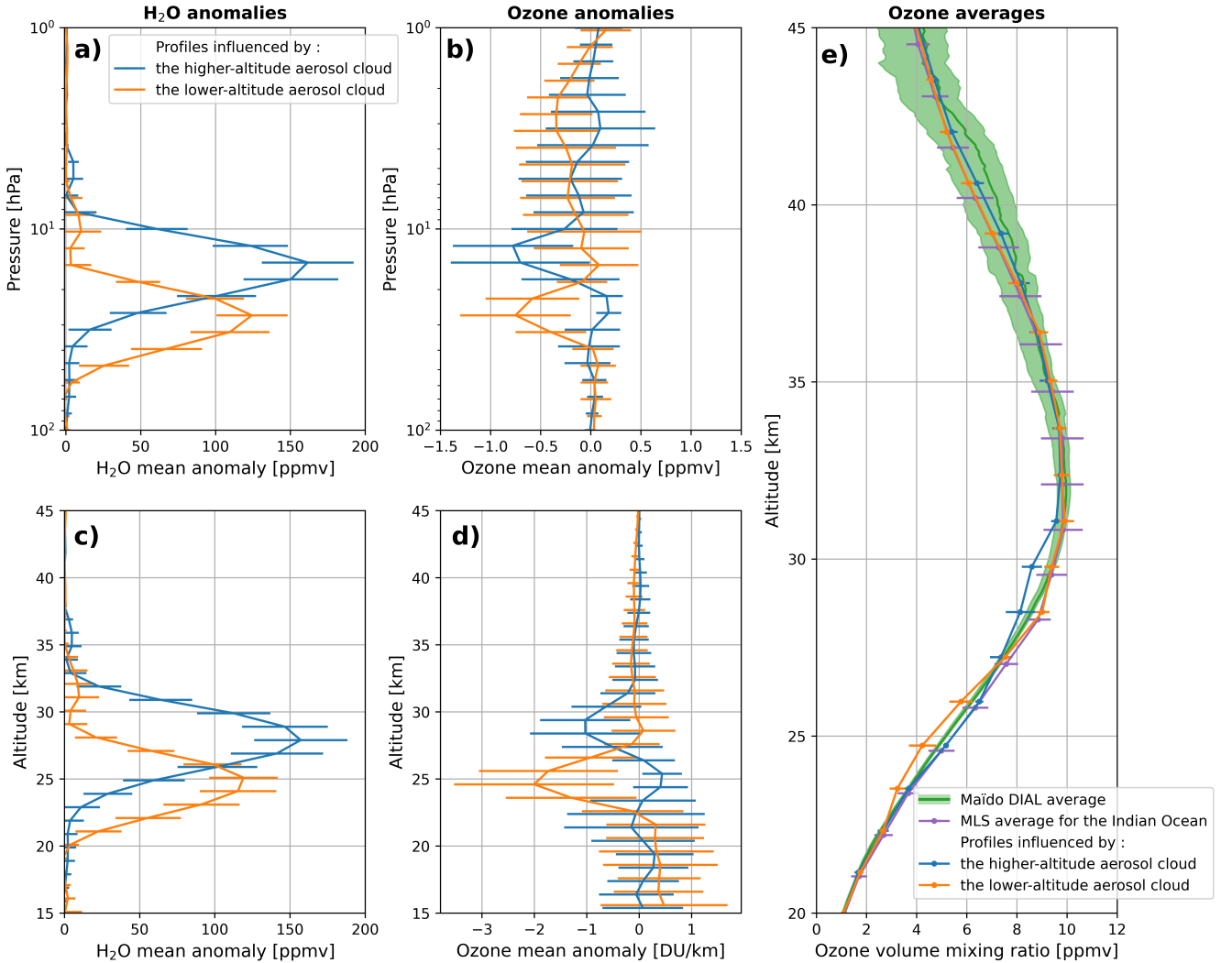
Figure 6. Mean anomalies and $\pm 1\sigma$ standard deviation (horizontal bars) in (**a-c**) water vapor and (**b-d**) ozone from v4 MLS profiles that met the selection criterion. Panels (**a-b**) present measurements from raw profiles in volume mixing ratio over a pressure range, while panels (**c-d**) show the same data over an altitude range, with ozone expressed in DU/km. Panel (**e**) displays the January mean lidar ozone profile with its $\pm 2\sigma$ standard deviation, the MLS average ozone profile for the Indian Ocean with its $\pm 1\sigma$ standard deviation, and the average v4 MLS ozone profiles influenced by the Hunga clouds with the corresponding $\pm 1\sigma$ standard deviation. Profiles influenced by the higher-altitude and lower-altitude clouds are displayed in blue and orange, respectively.
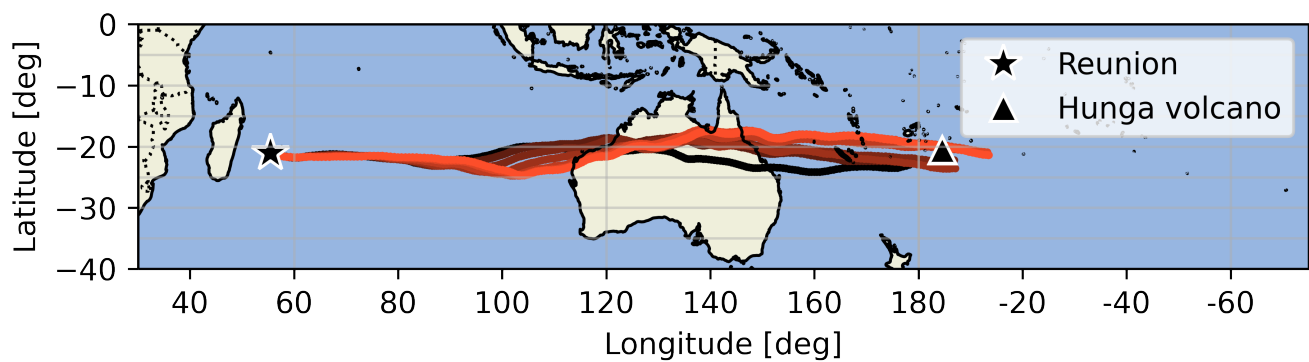
Figure 7. HYSPLIT back trajectories of 240 hours ending on 21 January at 00:00 UTC at the location of Saint-Denis, Reunion, between 23.5 and 29.0 km height. The star and triangle symbols indicate the ending point and the Hunga volcano location, respectively. The back trajectories are displayed with a color gradient, ranging from black for the trajectory ending at 23.5 km to orange for 29.0 km.
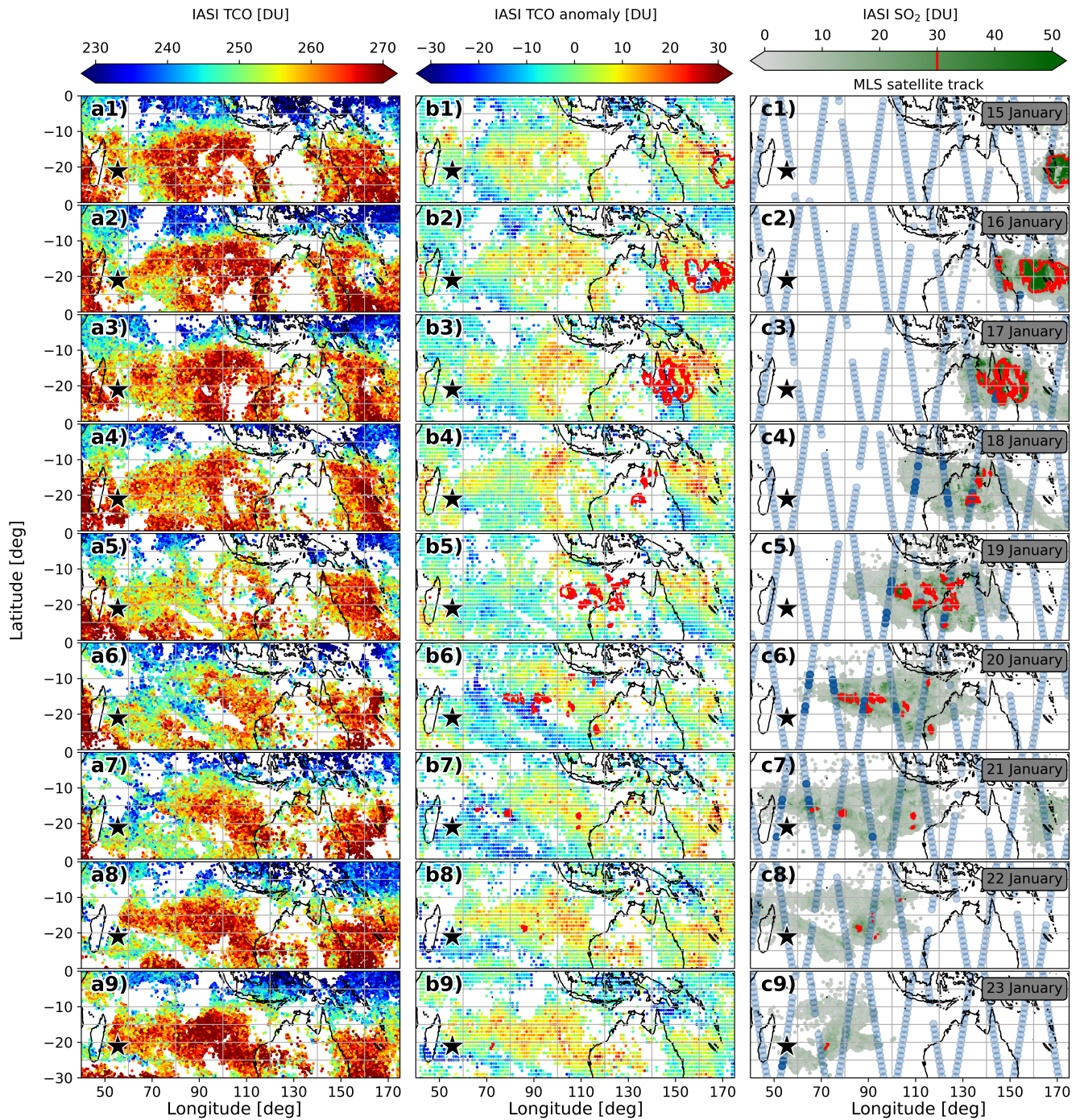
Figure A1. Daily evolution of (**a1-a9**) Total Column Ozone (TCO) and (**b1-b9**) TCO anomaly observed by IASI alongside (**c1-c9**) the satellite track of MLS (blue dots) and total SO_2 column from IASI between 15 and 23 January 2022. Dark blue dots on the MLS track represent the location of profiles meeting the Hunga-influenced selection criterion. The red contour indicates the regions where total SO_2 column is greater than 30 DU. The black and white star represents the location of Reunion. Each row corresponds to a distinct day, and the date of observation is indicated for each row in the right column. **31**